Improving the coherent quantum control of trapped ion qubits

Anders Lindberg

Master's Thesis in Physics,
Stockholm University
January 2, 2020

Supervisor: Markus Hennrich
Assistant supervisor: Gerard Higgins

Abstract

One of the challenges for quantum computing is the loss of coherence due to phase randomization introduced by noise. For quantum computers based on ion traps, coherence is limited by fluctuations in the magnetic field and by the linewidth of the laser used for qubit operations. This thesis is concerned with enhancing coherence by improving magnetic field stability with permanent magnets and building a test setup for reducing broadening of laser linewidth from optical fibers.

Previously coils were used to generate the magnetic field. Their stability is limited by the noise of the current drives. The coils have been replaced with permanent magnets in order to improve magnetic field stability. Two frames holding the permanent magnets in place were designed, 3D printed and then installed in the experiment. After installation Ramsey measurements were used to obtain $1/\sqrt{e}$ coherence times of $\tau_{sens} = (489 \pm 21)\,\mu s$ and $\tau_{insens} = (1540 \pm 80)\,\mu s$ for a more and less sensitive transition to magnetic fields between Zeeman sublevels of the qubit states, compared to $\tau_{sens} = (491 \pm 25)\,\mu s$ and $\tau_{insens} = (1254 \pm 53)\,\mu s$ when using the coils. From these results we were able to infer the root-mean-square (RMS) of the magnetic field and laser frequency fluctuations to be, both when the coils and permanent magnets were in use, $\sqrt{\overline{\Delta B^2}} \approx 110\,\mu G$ and $\sqrt{\overline{\Delta\omega^2}}/2\pi \approx 100\,Hz$, respectively. We were not able to improve coherence times, most likely due to the lack of magnetic field shielding from other noise sources in and outside the lab.

Optical fibers can broaden the linewidth of a laser by picking up environmental disturbances, such as vibrations and thermal fluctuations. A test setup for canceling the broadening of laser linewidth from fibers was built using active compensation. It has been tested by artificially introducing noise into the laser via the fiber, and we were able to successfully cancel the noise up to a few kHz.

Contents

Chapter 1

Introduction

Quantum computers have been a subject of great interest over the last few decades. They are based on the idea of performing computations using the principles of quantum mechanics, which is a radically different approach then for classical computers. Many different architectures [1] have been proposed, ion traps being one of the more promising ones. By trapping ions in ultrahigh vacuum and manipulating their electronic state with lasers, quantum computations can be performed. The degeneracy of the electronic states are lifted using a magnetic field. In our experiment, we trap strontium ions of isotope $^{88}Sr^{+}$ as described in section 2.2.

Most quantum computing architectures are based on two-level quantum systems called qubits, for which the states are denoted $|0\rangle$ and $|1\rangle$ and are used to represent bits of information with value 0 and 1, in analogue to classical computers. Since a qubit is a quantum system, it also possible to prepare superposition states of $|0\rangle$ and $|1\rangle$, and multiple qubits can also be entangled. These are important properties for quantum computing, they are the differentiating factors from classical computers. For trapped ion qubits, $|0\rangle$ and $|1\rangle$ are encoded using electronic states.

Quantum systems are sensitive to the environment. In particular, noise can have a significant detrimental effect on quantum computations, which depends on a well defined phase between $|0\rangle$ and $|1\rangle$. Noise can introduce random phase between $|0\rangle$ and $|1\rangle$, a phenomenon known as *dephasing*, and as a result, the system gradually loses information about the superposition states. This is one type of *decoherence* in a quantum system. The timescale over which a well defined phase between $|0\rangle$ and $|1\rangle$ can be maintained is called the *coherence time*. Different qubit architectures may differ in what causes decoherence, but the underlying principle of dephasing is the same. For ion traps, two prominent sources of decoherence are magnetic field fluctuations and the linewidth of the laser manipulating the qubit states. Improving magnetic field stability and reducing the laser linewidth to improve coherence times are the topic of this thesis.

Previously, before this thesis, pairs of coils were used to generate the magnetic field of the ion trap. Due to fluctuations in current, the magnetic field may fluctuate. For this reason, we have replaced the coils with permanent magnets, as this has been shown to improve coherence times in other groups[2]. However, it should be noted that without a magnetic field shielding to protect against external magnetic field noise we do not expect a large, if any, improvement in coherence times.

Additionally the fiber used to transport laser light to the experiment can introduce phase noise into the laser light due to vibrations or thermal fluctuations. This has been successfully handled before with *fiber noise cancellation*, and so we have built a test setup as a first step to implement this in the experiment.

The thesis follows the following structure.

- In chapter 2 we provide a *brief overview of quantum computing with trapped ions*.
- *Permanent magnets*: Chapter 3 is dedicated to developing a theoretical model for the permanent magnets. This model is used in chapter 4, where we describe the design and manufacture of a pair of frames for permanent magnets. In chapter 5 we characterize the magnetic field generated by the magnets. The installation of the permanent magnets as well as the results are described and presented in 6, followed by a discussion in chapter 7.
- *Fiber noise cancellation*: The test setup for fiber noise cancellation is described and then characterized in chapters 8 and 9. The results are then discussed in chapter 10.
- The *summary and outlook* can be found in chapter 11.

Chapter 2

Quantum computing using trapped ions

This chapter describes the basics on how to use trapped ions for quantum computation, as well as some limiting factors that need to be overcome.

2.1 Quantum computation

The smallest unit of information that can be encoded in a classical computer is that of a *bit*, which can be either 0 or 1. More complex information, such as numbers or funny pet videos, are constructed by multiple bits. For a quantum computer, the equivalent[1] to the bit is the *quantum bit*, or *qubit*. A qubit is a two level quantum system, where each level is used to store $|0\rangle$ or $|1\rangle$. These states are the basis of the qubit state. A general state $|\psi\rangle$ of a qubit is a superposition of $|0\rangle$ and $|1\rangle$

$$|\psi\rangle = c_0|0\rangle + c_1|1\rangle \tag{2.1}$$

where c_0 and c_1 are complex numbers subject to the normalization condition $|c_0|^2 + |c_1|^2 = 1$.

For multiple qubits the general state $|\Phi\rangle$ becomes more complicated due to entanglement. With N qubits $|\Phi\rangle$ is then a superposition of product states[3], which are just tensor products between the individual qubit states. This include entangled states, which cannot be written as product states but can be written as superpositions of product states. As an example, for 2 qubits the general state is

$$|\Phi\rangle = c_{00}|0\rangle \otimes |0\rangle + c_{01}|0\rangle \otimes |1\rangle + c_{10}|1\rangle \otimes |0\rangle + c_{11}|1\rangle \otimes |1\rangle. \tag{2.2}$$

where c_{ij} are normalized complex coefficients for which $\sum_{i,j} |c_{ij}|^2 = 1$. For a N qubit state there are 2^N product states and the general state $|\Phi\rangle$ can be constructed by a linear combination of these.

Entangled states have no classical equivalent, and cannot be efficiently represented on a classical computer. This is because the number of terms required to store a N qubit state on a classical computer scales exponentially as 2^N. For algorithms and computational problems that take advantage of entanglement and also superposition states, it is possible to achieve an exponential speedup compared to classical computers. Examples include Shor's algorithm, but also simulations of quantum systems.

2.1.1 Dephasing and coherence

Quantum computing relies on *coherent superposition states*, which means that there must be a well defined amplitude and phase relation between c_0 and c_1, and thus $|0\rangle$ and $|1\rangle$, in equation (2.1). The amplitude and phase relation between c_0 and c_1 deteriorate over time due to various processes. Of particular importance to this thesis are *dephasing processes*[1] which introduces a random phase difference ϕ between $|0\rangle$ and $|1\rangle$ which accumulates over time while preserving population and energy. We can write this as

$$|\psi\rangle = c_0|0\rangle + e^{i\phi}c_1|1\rangle. \tag{2.3}$$

Dephasing can be caused by phase noise affecting the system and is problematic since it means we lose information about the relative phase between $|0\rangle$ and $|1\rangle$.

This can be illustrated by considering the Bloch sphere, as in figure[2] 2.1 for a qubit state $(|0\rangle + |1\rangle)/\sqrt{2}$. Dephasing causes us to lose track of the azimuthal position of the Bloch vector in the equator. Since ϕ accumulates over time, more and more information is lost as time passes until we finally reach a situation where we have no information left about the relative phase. We then cannot predict where the Bloch vector ends up after a series of qubit operations. Practically this means that the system evolves from a coherent superposition state into a *statistical mixture*. Experimentally this means that each time a series of qubit operations is performed, the final state will be different. How different just depends on how much random phase ϕ has been accumulated.

The characteristic timescale over which this happens is known as the *coherence time*, and the loss of coherence is typically referred to as *decoherence*. It should be noted that decoherence refers to any loss of coherence, and not just loss of coherence due to dephasing.

Longer coherence times means we can perform longer quantum computations before we lose too much information due to decoherence. To calculate coherence times a noise model is needed, such as the one derived in section 6.3.

[1] One example of a different kind of decoherence process is population decay.
[2] The Python package *QuTIP* was used to plot these and all other Bloch spheres in this thesis.

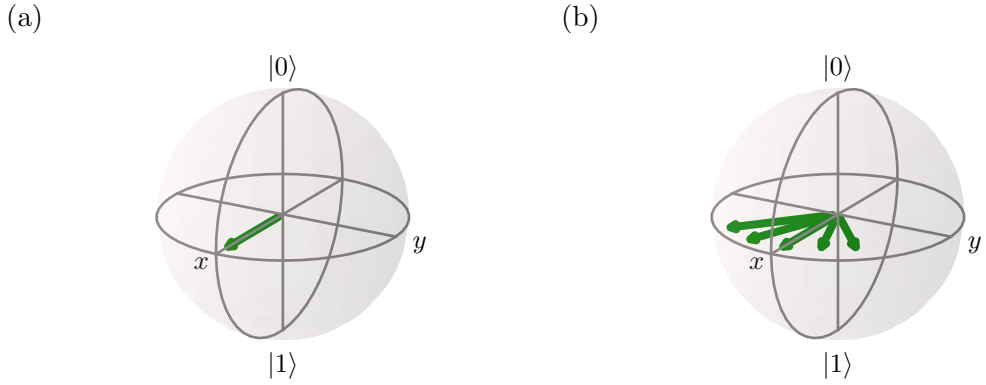

Figure 2.1: A qubit on the Bloch sphere, first (a) initialized to $(|0\rangle + |1\rangle)/\sqrt{2}$ at time $t = 0$ and then left alone. Due to noise it accumulates a random phase ϕ, so (b) at time t the qubit state is $(|0\rangle + e^{i\phi}|1\rangle)/\sqrt{2}$. This is shown as a spread of the Bloch vector, since the accumulated ϕ will be different every time the experiment is repeated. For longer times t, more phase can accumulate and thus we begin to lose track of the azimuthal position of the Bloch vector.

2.2 Trapped ions qubits

In our experiment, we represent qubits by encoding $|0\rangle$ and $|1\rangle$ using Zeeman sublevels of the metastable[3] $4D_{5/2}$ and and the ground state $5S_{1/2}$ of strontium $^{88}Sr^{+}$ ions. A level scheme can be found in figure 2.3. The ions, each of which represent a single qubit, are stored in a linear Paul trap[4][5]. The ions can then be manipulated using resonant laser pulses from a 674 nm laser, which can be used to implement quantum gate operations.

A linear Paul trap uses an oscillating electric quadrupole field generated by 4 electrodes parallel to a common trap axis z to keep ions trapped for long periods of time. This is depicted in figure 2.2(a). One pair of the parallel electrodes are at a DC voltage V_{DC} while the other has an oscillating voltage V_{RF}. This creates an effective electric potential confining ions to the trap axis[4], typically in form of a 1D ion string. End cap electrodes aligned with the trap axis confines the ions in axial direction and allows adjustment of ion positions. Since collisions with atoms in air are detrimental, the ion trap is required to be in ultra-high vacuum conditions and is thus placed in a vacuum vessel. For details about the ion trap and vacuum vessel, see the master thesis of Fabian Pokorny[6].

The magnetic field that splits the $4D_{5/2}$ and $5S_{1/2}$ into Zeeman sublevels were previously generated by a pair of coils on either side of the vacuum vessel, as

[3]Metastable simply means that it decays slowly enough that it is effectively stable. The spontaneous lifetime of the $4D_{5/2}$ level is $\tau = 0.45\,\mathrm{s}$.

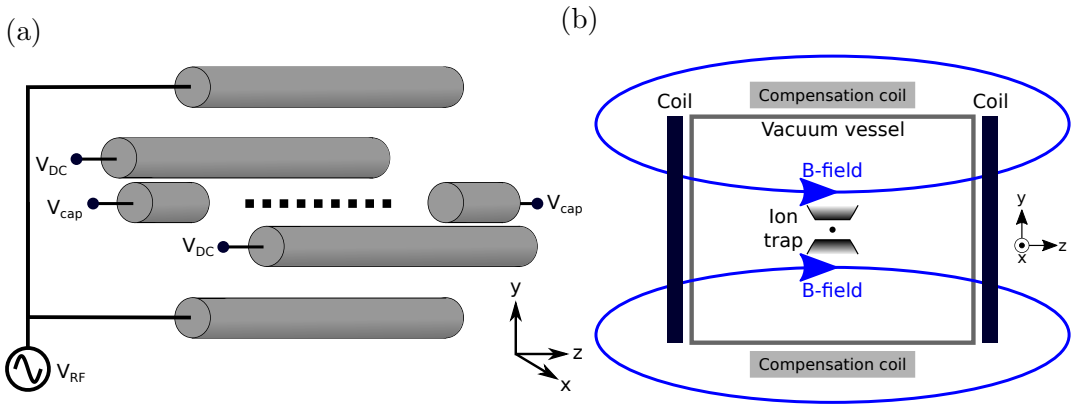

Figure 2.2: Schematic (a) of the linear Paul trap, where two electrodes oscillate with an AC voltage V_{RF}, while the other two as well as the end cap electrodes are kept at DC levels V_{DC} and V_{cap}, respectively. Trapped ions are sketched as dots. (b) Schematic of the trap inside the vacuum vessel, with a magnetic field along the z-axis generated by the coils. The compensation coils generate a weak magnetic field along the y-axis to cancel constant external fields. An additional pair of compensation coils cancels the DC magnetic field along the x-axis, but are not shown here.

depicted in figure 2.2(b). Two additional coil pairs, aligned with the x- and y-axis, are used to compensate for constant external magnetic field components. They generate much weaker magnetic fields. In this thesis they are called *compensation coils*.

Trapped ion qubits are promising due to being well controlled quantum systems. Additionally they are identical, free from imperfections introduced in man-made qubits during manufacturing.

2.2.1 Dephasing and improving coherence times

As discussed in section 2.1.1, phase noise affecting the system can cause dephasing and loss of coherence. In the case of quantum computation with ion traps, two well known sources of dephasing are magnetic field fluctuations and laser phase noise introduced by optical fibers, also known as fiber noise, for the qubit transition.

We can model the effects of the phase noise as phase flip operations[1], using a time dependent detuning in the Hamiltonian[7] $\hat{H}_{noise}(t) \propto \Delta E(t)\hat{\sigma}_z$. Here $\Delta E(t)$ represents the energy fluctuation corresponding to the phase noise and the Pauli operator $\hat{\sigma}_z$ the phase flip operation. For magnetic field fluctuations ΔB, the Zeeman effect introduces an energy fluctuation $\Delta E(t)$. In case of laser phase noise, phase fluctuations affects the qubit operations and can be modeled as

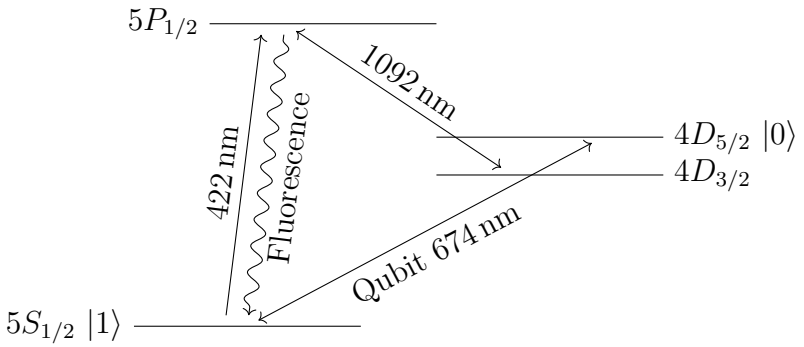

Figure 2.3: Energy level diagram of strontium. The $5S_{1/2}$ state is used to encode $|1\rangle$ while $4D_{5/2}$ encodes $|0\rangle$. The $5S_{1/2} \leftrightarrow 4D_{5/2}$ transition is addressed with the 674 nm qubit laser. Other relevant energy levels include $5P_{1/2}$ and $4D_{3/2}$, which are used for state detection. See section 6.2.2 for more information.

random frequency detunings $\Delta\omega(t)$. Then the corresponding energy fluctuation is $\Delta E(t) = \hbar\Delta\omega(t)$. Both of these effects thus affect the system via $\hat{H}_{noise}(t)$. This is described in more detail in section 6.3.

Magnetic field fluctuations can be caused by surrounding electronics. The coils generating the quantization magnetic fields are no exceptions, since small current fluctuations cause magnetic field fluctuations that can limit coherence times. By replacing these coils with permanent magnets[2], other groups have realized more stable magnetic fields and coherence times have increased as a result. They also found that magnetic field shielding is required for larger then marginal gains in coherence times, since magnetic fields from other electronics or labs can contribute significantly to decoherence. Installation of such a shield is beyond the scope of this thesis.

No laser is perfectly monochromatic, but just has a very narrow linewidth compared to other light sources. The linewidth of the laser depends on many factors, such as temperature, acoustic noise or even the Schawlow-Townes limit of laser linewidth. Most importantly for this thesis, the phase noise introduced by optical fibers have a broadening effect of the laser linewidth.

The phase noise of the 674 nm qubit laser comes from two fibers. The vacuum vessel containing the ion trap and the 674 nm laser are on different optical tables, and a 10 m long fiber is used to transport the laser light to the right optical table. Furthermore, the laser frequency is locked to an optical reference cavity using a Pound-Drever-Hall lock[8]. This requires the optical cavity to be stored in a very stable temperature and vibration free environment, and it is thus placed in a box specifically built with this in mind. A 20 m long fiber is used to transport the light from the laser to the cavity. Both of these fiber contribute to introduction of phase

noise. To compensate for this, active cancellation schemes have been developed[9], commonly referred to as *fiber noise cancellation*. For this thesis a test setup for fiber noise cancellation has been developed.

Chapter 3

Theory for permanent magnets

3.1 Introduction

In the trapped ion experiment two coils were previously used to generate a homogeneous magnetic field. We would like to generate a low noise magnetic field using permanent magnets. The magnetic field should be directed along the trap axis and be as homogeneous as possible at the region where the ions reside. This can be achieved by having two frames of a suitable material holding the magnets in a circular configuration at a specific radius. Each of these frames will be placed on either side of the vacuum vessel containing the ion trap, replacing the coils and aligned so they are centered on the trap axis. In other words, they are in *coaxial geometry*.

In this chapter we will describe the underlying theory, which motivates the chosen separation and radius of these frames.

3.2 Magnets as magnetic dipoles

In order to calculate the magnetic field generated at and around the position of the trapped ions, we assume that the magnets are far away from the ion trap and that their spatial dimensions are small. We also assume that the surrounding environment will not affect the magnetic field to a large degree. For example, this assumption entails the absence of metals that are magnetic or can be magnetized easily. This allows us to approximate the permanent magnets as magnetic dipoles.

Thus let us first consider the magnetic field $\vec{B}_d$ at a point P with position $\vec{r}_p$ due to a magnetic dipole at $\vec{r}_d$. The magnetic field at $\vec{r}_p$ will depend on the relative position $\vec{r}_p - \vec{r}_d$ to the dipole, as illustrated in figure 3.1. $\vec{B}_d$ is then given

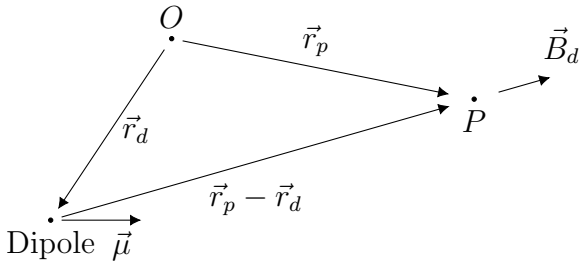

Figure 3.1: The magnetic field $\vec{B}_d$ at point P due to a magnetic dipole at $\vec{r}_d$ depends on the relative position $\vec{r}_p - \vec{r}_d$ and the magnetic dipole moment $\vec{\mu}$.

as [10][11]

$$\vec{B}_d(\vec{r}, \vec{r}_d) = \frac{\mu_0}{4\pi|\vec{r}_p - \vec{r}_d|^3}\left(\frac{3(\vec{r}_p - \vec{r}_d)(\vec{\mu}\cdot(\vec{r}_p - \vec{r}_d))}{|\vec{r}_p - \vec{r}_d|^2} - \vec{\mu}\right) \tag{3.1}$$

where μ_0 is the permeability of free space and $\vec{\mu}$ is the magnetic dipole moment of the dipole.

The magnitude μ of the magnetic moment depends on the volume V of a magnet as well as its remanence[1] B_r as[11]

$$\mu = \frac{VB_r}{\mu_0}. \tag{3.2}$$

While we are approximating the magnets as magnetic dipoles which have no spatial extent, we still use equation (3.2) to obtain their magnetic moment μ.

Now, if we have N dipoles instead of a single one, the total magnetic field at an arbitrary position is just the sum of the contributions from each dipole. Denoting the position and magnetic moment of the i:th dipole as $\vec{r}_{d,i}$ and $\vec{\mu}_i$, the magnetic field at $\vec{r}_p$ is given by

$$\vec{B}(\vec{r}_p) = \frac{\mu_0}{4\pi}\sum_{i=1}^{N}\frac{1}{|\vec{r}_p - \vec{r}_{d,i}|^3}\left(\frac{3(\vec{r}_p - \vec{r}_{d,i})(\vec{\mu}_i\cdot(\vec{r}_p - \vec{r}_{d,i}))}{|\vec{r}_p - \vec{r}_{d,i}|^2} - \vec{\mu}_i\right). \tag{3.3}$$

3.3 Generated axial magnetic field

Let us consider a pair of magnet holders, placed symmetrically along a common central axis z, in coaxial geometry. The magnet holders are separated by a distance Δ, and the magnets themselves are placed at a radius R. All of the magnets are oriented the same direction, such that their magnetic moment $\vec{\mu}$ is parallel to the

[1] See [12] for the definition of remanence.

z-axis. We choose the mid-point between the holders on the z-axis to be the origin. Each magnet is approximated as a dipole. Since all the magnets are oriented along the z-axis, the magnetic moment itself is $\vec{\mu} = \mu\hat{z}$, where μ can be obtained from equation (3.2).

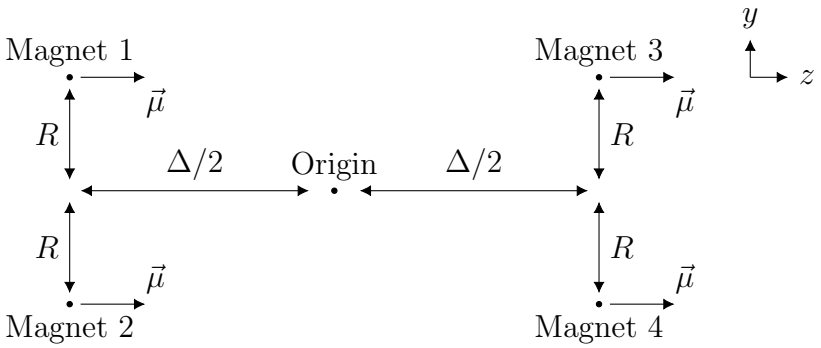

Figure 3.2: Simplified view of the magnet holders, with only four magnets.

The ions will be aligned along the z-axis, and thus we are only interested in the magnetic field along this axis. In order to simplify the analysis we will only consider a pair of magnets from each holder, residing in the yz-plane as illustrated in figure 3.2. Since the other magnets will just add more contributions, using all the magnets gives a result proportional to the four-magnet result as long as they are placed pairwise like in this simplified case.

Equation (3.1) yields the magnetic field for an arbitrary point at $\vec{r}_p$ due to magnet i at position $\vec{r}_{d,i}$. For our purposes we want to know the magnetic field along the z-axis, and thus we choose $\vec{r}_p = z\hat{z}$. The magnet positions $\vec{r}_{d,i}$ can be inferred from figure 3.2 to be $\vec{r}_{d,1} = (-\Delta/2)\hat{z} + R\hat{y}$, $\vec{r}_{d,2} = (-\Delta/2)\hat{z} - R\hat{y}$, $\vec{r}_{d,3} = (\Delta/2)\hat{z} + R\hat{y}$ and $\vec{r}_{d,4} = (\Delta/2)\hat{z} - R\hat{y}$. The relative positions $\vec{r}_i = \vec{r}_p - \vec{r}_{d,i}$ from the magnets to the chosen point are then

$$\vec{r}_1 = z\hat{z} - ((-\Delta/2)\hat{z} + R\hat{y}) = (z + \Delta/2)\hat{z} - R\hat{y}, \tag{3.4}$$
$$\vec{r}_2 = z\hat{z} - ((-\Delta/2)\hat{z} - R\hat{y}) = (z + \Delta/2)\hat{z} + R\hat{y}, \tag{3.5}$$
$$\vec{r}_3 = z\hat{z} - ((\Delta/2)\hat{z} + R\hat{y}) = (z - \Delta/2)\hat{z} - R\hat{y}, \tag{3.6}$$
$$\vec{r}_4 = z\hat{z} - ((\Delta/2)\hat{z} - R\hat{y}) = (z - \Delta/2)\hat{z} + R\hat{y}. \tag{3.7}$$

From these equations we can also see that magnets 1 and 2 are always at the same distance to the point z, since $|\vec{r}_1| = |\vec{r}_2|$. Similarly for magnets 3 and 4 we have $|\vec{r}_3| = |\vec{r}_4|$. As such we can define the corresponding distances r_L and r_R as

$$r_L = |\vec{r}_1| = |\vec{r}_2| = \sqrt{(z + \Delta/2)^2 + R^2}, \tag{3.8}$$
$$r_R = |\vec{r}_3| = |\vec{r}_4| = \sqrt{(z - \Delta/2)^2 + R^2}. \tag{3.9}$$

To obtain the total magnetic field $\vec{B}(z)$ along the z-axis we will add each holder individually.

First we consider the contribution $\vec{B}_L$ from magnets 1 and 2, to the left in figure 3.2. Using equation (3.3) and the magnetic moment $\vec{\mu} = \mu\hat{z}$ we obtain

$$\vec{B}_L = \frac{\mu_0 \mu}{4\pi r_L^3} \left(\frac{3}{r_L^2} \left[\vec{r}_1(\hat{z} \cdot \vec{r}_1) + \vec{r}_2(\hat{z} \cdot \vec{r}_2) \right] - 2\hat{z} \right).$$

Using equations (3.4) and (3.5) we find

$$\vec{r}_1(\hat{z} \cdot \vec{r}_1) + \vec{r}_2(\hat{z} \cdot \vec{r}_2) = 2(z + \Delta/2)^2 \hat{z}.$$

As we can see the components along the y-axis will cancel leaving us with only a component along the z-axis. Thus $\vec{B}_L$ becomes

$$\vec{B}_L = \frac{\mu_0 \mu}{2\pi r_L^3} \left(\frac{3(z + \Delta/2)^2}{r_L^2} - 1 \right) \hat{z}$$

The value of $\vec{B}_L$ at the common axis is shown in figure 3.3. We can here see an important difference from using coils, and that is that the magnetic field changes direction close to the magnet pair.

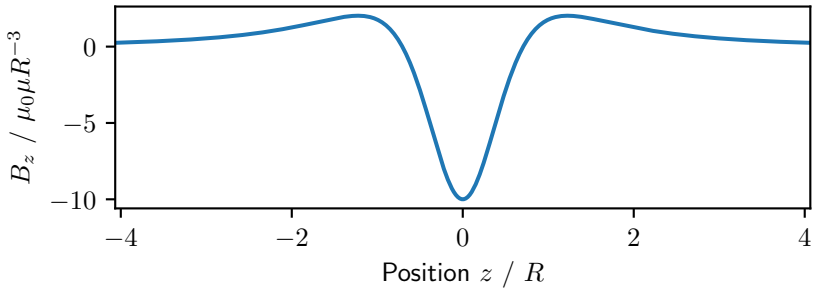

Figure 3.3: The magnetic field of a single holder.

Now consider the magnetic field contribution $\vec{B}_R$ due to magnets 3 and 4, on the holder to the right. We can use the same approach, but for magnets 3 and 4 as well as r_R instead of r_L. Doing this yields that $\vec{B}_R(z) = \vec{B}_L(-z)$, which is not surprising since we have only shifted the holder position compared to $\vec{B}_L$.

The total magnetic field $\vec{B} = \vec{B}_L + \vec{B}_R$ becomes

$$\vec{B} = \frac{\mu_0 \mu}{2\pi} \left[\frac{1}{r_L^3} \left(\frac{3(z + \Delta/2)^2}{r_L^2} - 1 \right) + \frac{1}{r_R^3} \left(\frac{3(z - \Delta/2)^2}{r_R^2} - 1 \right) \right] \hat{z} \tag{3.10}$$

where $r_L = \sqrt{(z + \Delta/2)^2 + R^2}$ and $r_R = \sqrt{(z - \Delta/2)^2 + R^2}$. We have also used that $(z - \Delta/2)^2 = (-z + \Delta/2)^2$ to write this slightly more compactly.

This is, however, only for four magnets. Practically we would not want 4 magnets due to symmetry issues. The results for N magnets can, however, be derived from this simplified case as long we can place these magnets pairwise like in the four magnet case. Thus for N magnets we get

$$\vec{B} = \frac{N\mu_0\mu}{8\pi}\left[\frac{1}{r_L^3}\left(\frac{3(z+\Delta/2)^2}{r_L^2}-1\right)+\frac{1}{r_R^3}\left(\frac{3(z-\Delta/2)^2}{r_R^2}-1\right)\right]\hat{z} \tag{3.11}$$

3.4 Helmholtz-like configuration

If we have a string of N ions in the ion trap, located at the center position, it is desirable that all N ions experience the same magnetic field. For a pair of coils this can be achieved using the *Helmholtz configuration*, where the radius R of the coils equals their separation Δ. Such a configuration yields a remarkably constant magnetic field between the coils. This is because at the center position between the coils, the inflection points of their magnetic fields overlap. This result can be obtained[12] by making a Taylor expansion around the central position, where $z = 0$. The symmetry of the setup will cause the odd terms to cancel. By choosing $R = \Delta$, we also cancel the second order term. This is what gives us a Helmholtz configuration for a pair of coils.

Now we consider the case with permanent magnets instead of coils and repeat the same procedure. We thus make a Taylor expansion of the magnetic field given in equation (3.10) around the center position at $z = 0$. Since $\vec{B}$ only has a component along the z axis, we only consider this component B_z. The terms of the Taylor expansion are

$$B_z(z) = B_z(0) + z\left.\frac{dB_z}{dz}\right|_{z=0} + \frac{z^2}{2}\left.\frac{d^2B_z}{dz^2}\right|_{z=0} + \frac{z^3}{6}\left.\frac{d^3B_z}{dz^3}\right|_{z=0} + \mathcal{O}(z^4) \tag{3.12}$$

where $\mathcal{O}(z^4)$ represents all higher order terms. The odd order terms vanish due to symmetry, leaving us with the second order term as the first non-constant term. Hence we seek a relationship between R and Δ that solves $d^2B_z/dz^2|_{z=0} = 0$ to get a Helmholtz-like configuration for permanent magnets. $d^2B_z/dz^2|_{z=0}$ is given by

$$\left.\frac{d^2B_z}{dz^2}\right|_{z=0} = \frac{3\mu_0\mu}{32\pi\left(R^2+\frac{\Delta^2}{4}\right)^{5/2}}\left(\frac{35\Delta^4}{\left(R^2+\frac{\Delta^2}{4}\right)^2}-\frac{120\Delta^2}{R^2+\frac{\Delta^2}{4}}+48\right) \tag{3.13}$$

We want to find Δ in terms of R such that

$$\frac{3\mu_0\mu}{4\pi}\left(\frac{35\Delta^4}{8\left(R^2+\frac{\Delta^2}{4}\right)^{9/2}}-\frac{15\Delta^2}{\left(R^2+\frac{\Delta^2}{4}\right)^{7/2}}+\frac{6}{\left(R^2+\frac{\Delta^2}{4}\right)^{5/2}}\right) = 0. \tag{3.14}$$

There are 4 solutions to this equation. Of these, the two positive solutions are

$$\Delta_\pm = R\sqrt{6 \pm \sqrt{30}}. \tag{3.15}$$

The other two solutions are $-\Delta_\pm$ and thus does not contribute any more information. These negative solutions just switch the places of the holders.

The separations $\Delta_\pm$ corresponds to when the two inflection points of the magnetic fields $\vec{B}_L$ and $\vec{B}_R$ of the left and right magnet holder overlap at the center position. The solutions $\Delta_\pm$ are shown in figure 3.4, where equation (3.11) was used to calculate the axial magnetic field B_z. We can see that the two solutions correspond to a small separation and a large separation. The larger separation Δ_+ seems to also give a wider region where the axial magnetic field B_z is flat, compared to the smaller separation Δ_-. Do note that the position in figure 3.4 is expressed in units of R while B_z is in units of $\mu_0\mu/R^3$.

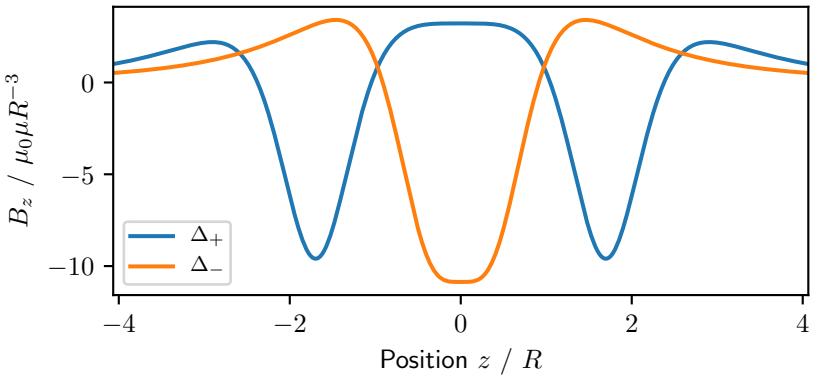

Figure 3.4: Axial magnetic field B_z for the two magnet holder separations $\Delta_\pm = R\sqrt{6 \pm \sqrt{30}}$, where R is the radial magnet position.

Now we consider what happens when the separation is either too large or too small compared to either of $\Delta_\pm$. The axial magnetic field B_z will have undesired magnetic field curvatures. To illustrate this, figure 3.5 shows B_z for a separation a bit larger and smaller then Δ_+. As previously, B_z was obtained from equation (3.11). We can see that a larger separation gives a local minima at $z = 0$, while a smaller separation gives a local maximum. In particular, the magnetic field changes faster then before with a quadratic dependence around $z = 0$.

3.5 Inhomogeneities in the xy-plane

Since we are using a finite number of discrete magnets the generated magnetic field might have undesired inhomogeneities. For this reason, many magnets are preferable to few magnets. Let us illustrate this now, with a couple of examples.

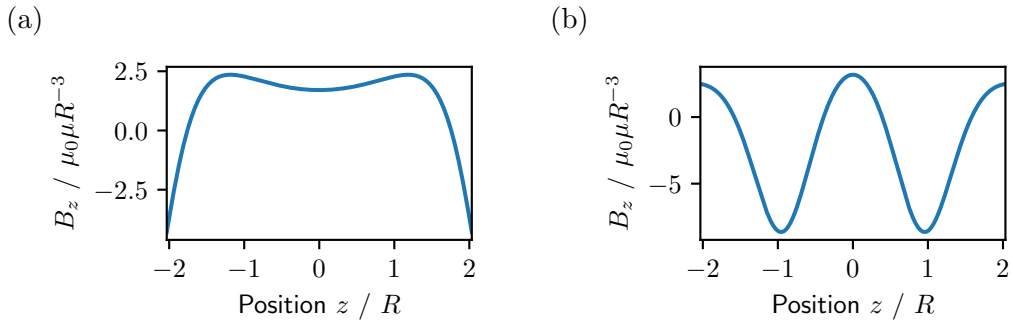

Figure 3.5: The axial magnetic field B_z when the separation is (a) too large or (b) too small compared to Δ_+ to give a Helmholtz-like configuration.

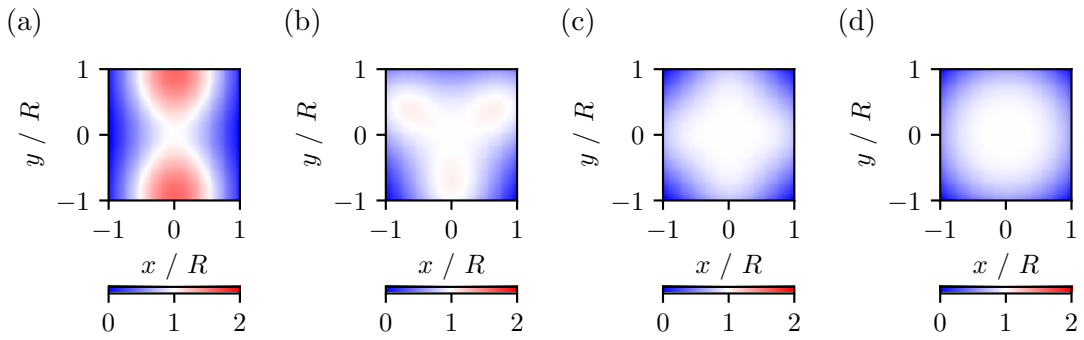

Figure 3.6: B-field amplitude in the xy-plane for (a) two, (b) three, (c) four and (d) 20 magnets per magnet ring. The B-field amplitude is normalized so the center position has value 1. Red indicates that the magnetic field strength is larger then the center position, and blue indicates it is smaller.

Suppose, for instance, we have two or three magnets per magnet ring. These magnets are placed at a radial distance to the z axis of R, and the rings are separated by $\Delta = R\sqrt{6+\sqrt{30}}$. We can then calculate the amplitude of the B-field in the xy-plane at $z = 0$ with equation (3.3). Here the x-axis is perpendicular to both the y-axis and the z-axis. The position of the n:th magnet can be obtained as $x = R\cos\theta_n$, $y = R\sin\theta_n$ and $z = \pm\Delta/2$ depending on the magnet holder. If there are a total of N magnets then $\theta_n = 2\pi(n-1)/N$. The resulting normalized B-field amplitude in the xy-plane is shown in figure 3.6 for two, three, four and 20 magnets.

We can illustrate the homogeneity by considering the B-field amplitude at a radial distance r_c from the center position in the xy-plane. In other words, we use equation (3.3) to calculate the magnetic field strength at positions $x = r_c\cos\theta$, $y = r_c\sin\theta$, $z = 0$ for a large number of angles θ. The fractional variation $(B - \langle B\rangle)/B$ of the B-field amplitude $B = |\vec{B}|$ is shown in figure 3.7(a) as a function of θ with

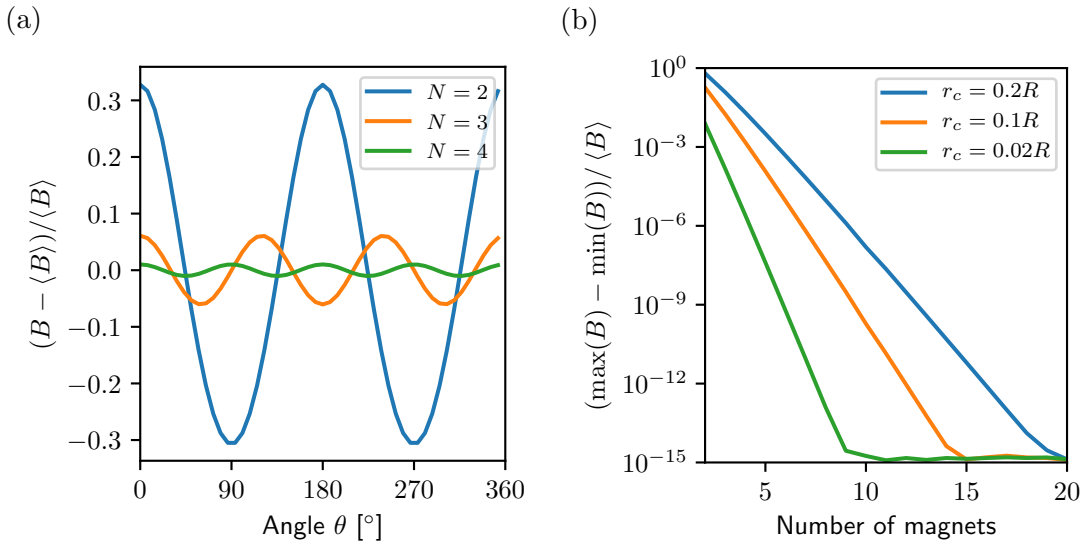

Figure 3.7: The (a) fractional variation $(B - \langle B\rangle)/\langle B\rangle$ as a function of angular position at a radius $r_c = 3\,\text{cm}$ for $N = 2, 3, 4$ magnets. The (b) oscillation contrast of the fractional variation as a function of magnet count, for $r_c = 1, 2, 3$ cm.

$r_c = R/5$ and for $N = 2, 3, 4$ magnets. There is an oscillating behaviour where the B-field amplitude is largest close to the magnets and smallest between two magnets. We also see that the oscillation contrast decreases with more magnets, indicating that the magnetic field becomes more homogeneous with more magnets. The contrast of the fractional variation is shown in figure 3.7(b) as a function of the number of magnets N for $r_c = R/5, R/10, R/20$. It decays exponentially as the number of magnets increases. We can also see that this exponential decay is faster for smaller r_c, indicating that the magnetic field also becomes more homogeneous closer to the center position. The exponential decay stops at $\approx 10^{-15}$ due to numerical issues with the simulation.

Chapter 4

Magnets and magnet holders

This chapter describes the design and manufacture of a pair of frames for the permanent magnets, as well as what kind of permanent magnets were chosen.

4.1 Permanent magnets

The magnets we used were Samarium-Cobalt magnets, specifically Sm_2Co_{17}. This material was chosen since it has already been used by other groups, who obtained good results [2], and for its good temperature stability of $-0.03\,\%/\mathrm{K}$. The magnets themselves are cylindrical with a diameter of 4 mm and a length of 6 mm. According to the manufacturer[1] they should have a remanence of $B_r \geq 1\,\mathrm{T}$. These magnets are quite small and we need many of them to generate the magnetic field used in the experiment, however, they were chosen with the idea that a larger number of magnets would create a more homogeneous magnetic field.

4.2 Design constraints for the magnet holders

At either side of the vacuum vessel there is a few cm of space where the magnet holders can be physically fit before other parts of the experimental setup get in the way. The coils could be separated by 200 mm to 250 mm. Due to the spatial constraints a Helmholtz configuration for coils was not possible, since the radii of the coils would be too large for them to fit amongst the surrounding equipment.

For the magnet holders, we chose to have a separation of 250 mm, which according to equation (3.15) means the magnets should be placed at a radius of $\approx 73.8\,\mathrm{mm}$ for a Helmholtz-like configuration.

[1] IBS Magnet.

The magnetic field generated by the coils was $\approx 3.6\,\mathrm{G}$ at the position of the ion in the ion trap, with a current of $I \sim 1\,\mathrm{A}$. It was desirable to have a similar or slightly lower magnetic field for efficient Doppler cooling. From equation (3.2), assuming the magnet dimensions given above, a remanence of $B_r = 1\,\mathrm{T}$, and equation (3.3) we can calculate that for 80 magnets per holder we should get about $\approx 3.2\,\mathrm{G}$ at the center position.

4.3 Magnet holder design

To hold the magnets in place a pair of magnet holders, illustrated in figure 4.1, was designed to be fitted on the sides of the vacuum chamber containing the ion trap. They are mounted at the same place as the coils they replace.

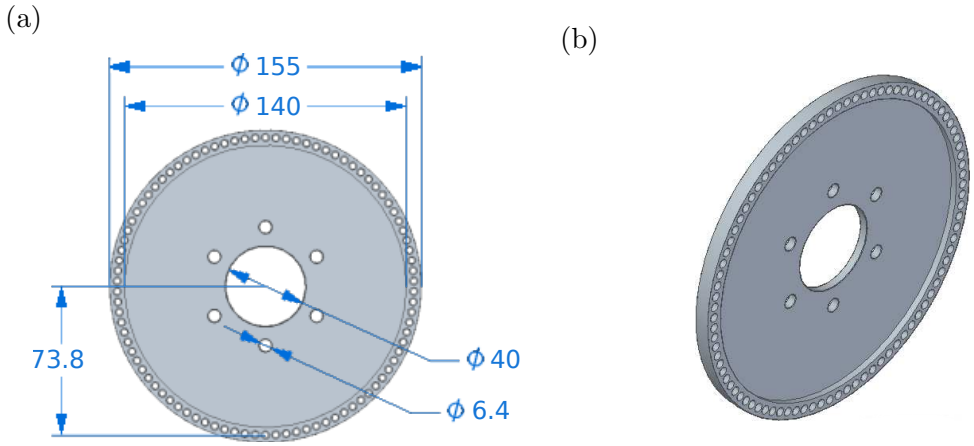

Figure 4.1: The CAD drawing of the magnet holders, both (a) with and (b) without the dimensions marked. The dimensions are in mm.

The magnet holders have a diameter of 155 mm, and a thickness of 7 mm. At a radial distance of 73.8 mm from the center there are 90 holes in which the magnets can be placed, which included 10 extra holes to allow some fine-tuning of the magnetic field strength if necessary. These holes have a diameter of 4.2 mm and a depth of 6 mm. At the end of these holes we designed narrower holes 3 mm in diameter, to make it easier to remove the magnets if needed. The dimensions of the holders are shown in figure 4.1(a) and the dimensions of the magnet holes are shown in figure 4.2(b).

The inner region of the holders are 3 mm thinner for easier mounting. At the center there is a large hole 40 mm in diameter to allow optical access for the on-axial laser beams. The holders are mounted using 6 screw holes around the center hole.

(a) (b)

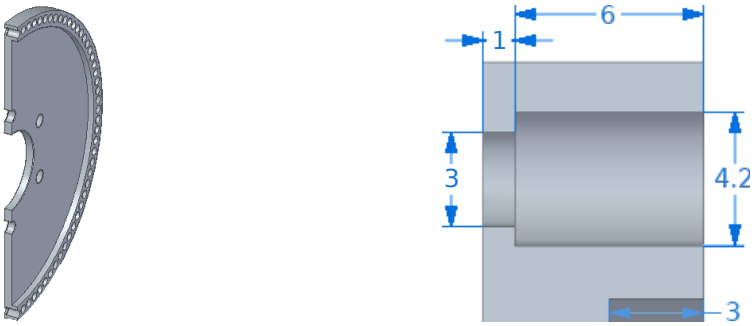

Figure 4.2: Cut through (a) of the magnet holder, as well as (b) a detailed view of the magnet holders. All given dimensions are in mm.

Keep in mind that to avoid inhomogeneities and non-axial components in the magnetic field the magnets should be inserted pairwise so each magnet has another magnet on the other side of the holder. They should also be evenly distributed over the holders. For the 80 magnets we left every 9:th magnet hole empty, which should create a fairly homogeneous magnetic field. Imperfections in holder construction, position and orientation can naturally introduce inhomogeneities or non-axial components in the magnetic field.

4.4 Manufacturing the magnet holders

The magnet holders were 3D printed using PLA plastic. The reasons 3D printing was chosen were two-fold. First reason was to enable faster design and testing of the magnet holders. Second, this technique has been implemented successfully by the ion trap group in Berkeley [13] and appears to have worked well for them, so it may be a cheaper and faster way to replace the coils with permanent magnets compared to manufacturing these holders from something like aluminium. Aluminium, however, may provide better structural and thermal stability.

For each holder, the magnets were inserted so their north and south poles were all pointing in the same direction. When put on the vacuum vessel the holders would also be placed so their north and south poles points in the same direction. With the right separation and alignment this should generate a Helmholtz-like magnetic field. The resulting magnet holders with their magnets inserted are shown in figure 4.3. To make it easier to see which holder is which, the holders were labeled as holders 1 and 2.

Due to imperfections in manufacturing, some of the magnets were hard to insert while others had to be glued to stay in their holes. Additionally, some of

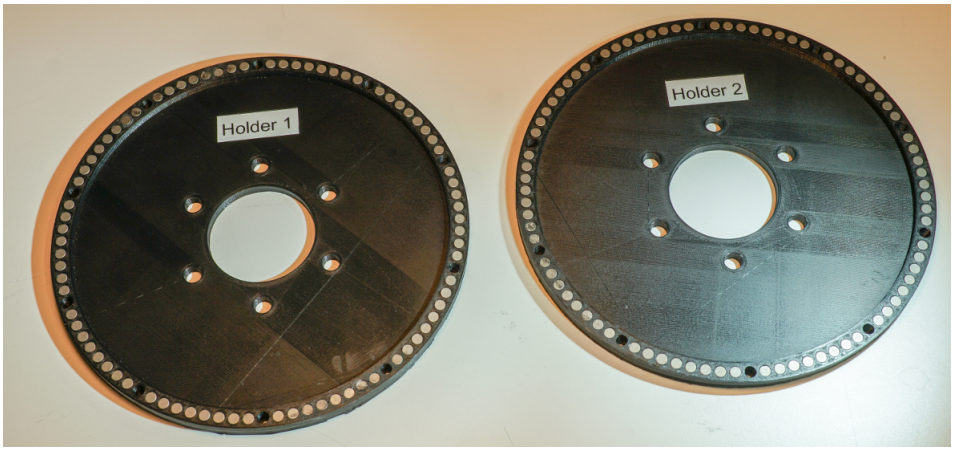

Figure 4.3: The magnet holders with 80 magnets inserted.

the magnets ended up tilted outwards at a slight angle. This was not the case for all magnets, as can be seen in figure 4.4.

(a) (b)

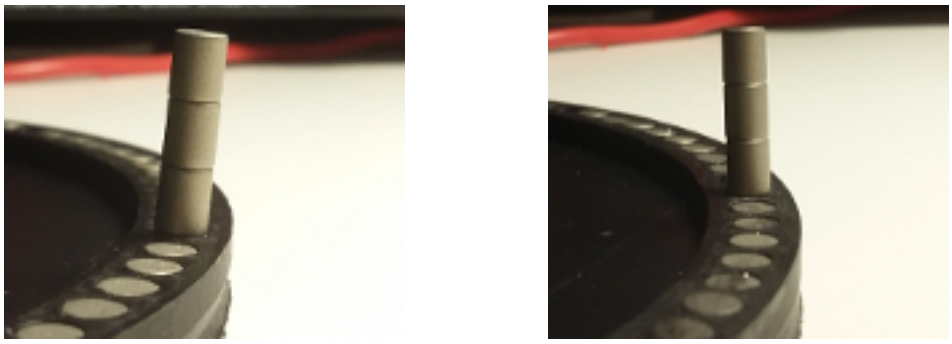

Figure 4.4: Tilted (a) and untilted (b) magnets in one of the magnet holders.

Chapter 5

Magnetic field characterization

Before installing the permanent magnets around the ion trap, their magnetic field was characterized in a test setup. This was to check if the magnetic field generated by the permanent magnets had desirable properties. It was also intended to test the theory developed in chapter 3. This chapter describes the experimental setup used to characterize the magnetic field and presents the results.

5.1 Experimental setup

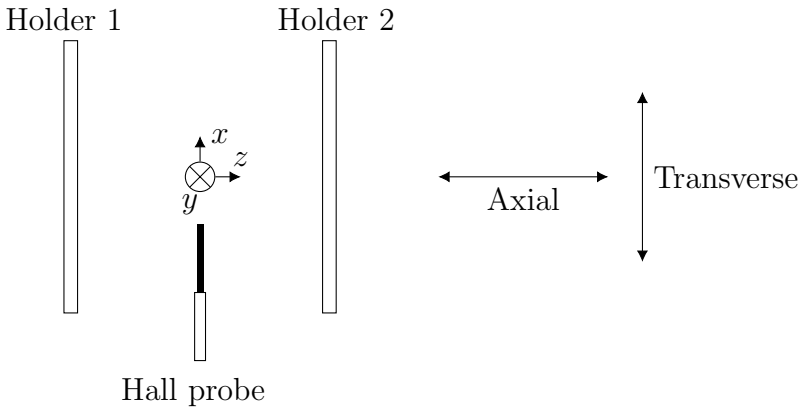

Figure 5.1: Illustration of the Hall probe placed between the magnet holders. The arrows marked *axial* and *transverse* shows the direction the Hall probe moves during the two types of measurements.

To characterize the magnetic field we placed the magnet holders in coaxial geometry and used a Hall probe[1] to measure the magnetic field strength between

[1]HU-ST1-184605 from Magnet-Physik. Computer controlled via USB.

them, as illustrated in figure 5.1. Two types of measurements were performed: Axial measurements, where the Hall probe was moved along the z axis, and transverse measurements, where it was moved along the x-axis. Due to symmetry we assumed the x-axis to be sufficient for the transverse measurements.

The Hall probe measures the magnetic field strength along one direction. It has a resolution of 0.1 G, an accuracy of 2 %. We took 100 measurements per position. Since the Hall probe only measures one component of the magnetic field, we would have to rotate it to the right angle 90° and repeat the measurements for each component we were interested in. From this data we calculated the mean and used the standard deviation as uncertainty. Since multiple datasets would be combines we would use error propagation [14] to determine the resulting uncertainty.

The positions for these measurements were read directly from the optical rail, with an uncertainty of $\delta z = \pm 2\,\mathrm{mm}$. To compare with theory we would estimate a midpoint z_0 between the holders, with an uncertainty of $\delta z_0 = \pm 1\,\mathrm{cm}$.

5.1.1 Axial characterization setup

For the axial measurements, the magnet holders were placed on platforms on an optical rail, separated by $\Delta = (25.0 \pm 0.2)\,\mathrm{cm}$. The Hall probe was attached to a mobile translation stage between the magnet holders. It could be moved along the axial direction. Three smaller translation stages on the mobile platform allowed fine tuning the Hall probe position. This setup is shown in figure 5.2. We only measured the z-component of the magnetic field in this case. With proper alignment the other components should cancel.

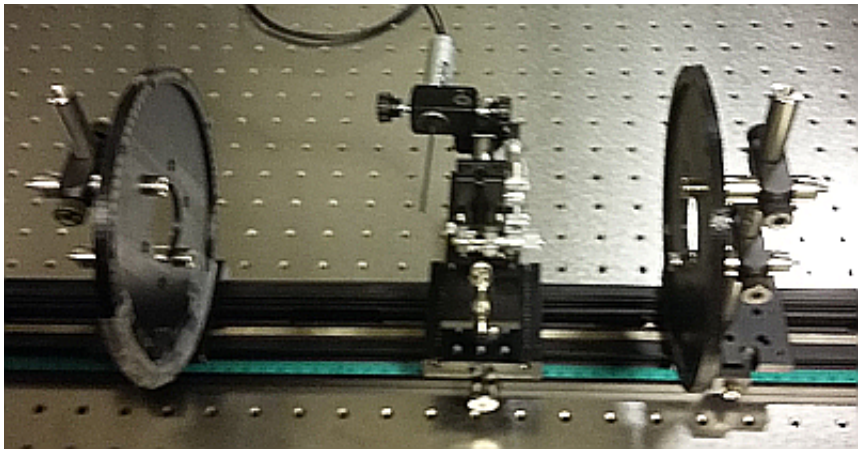

Figure 5.2: Experiment setup for axial characterization of the magnetic field.

5.1.2 Transverse characterization setup

For the transverse measurements, we would change the setup so the optical rail was aligned with the x-axis instead of the z-axis. This is shown in figure 5.3. In order to measure all components of the magnetic field, we mounted the Hall probe in two different ways, as depicted in figure 5.3.

(a) (b)

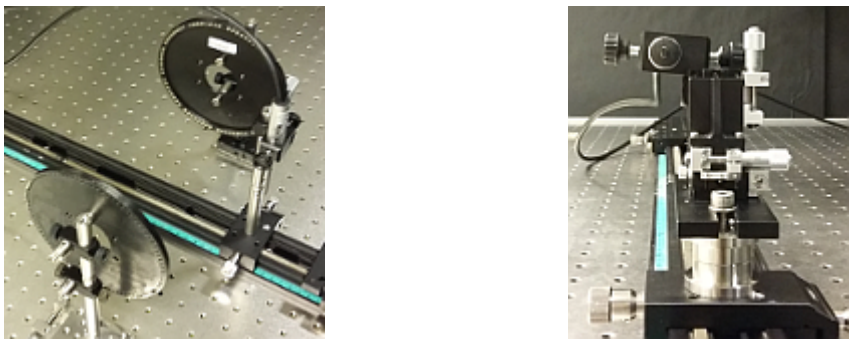

Figure 5.3: Experimental setup for transverse measurements of the magnetic field. To allow measurement of all components, the setup for holding the Hall probe in place was different for (a) measuring the x-component compared to (b) measuring the y- and z-components.

5.1.3 Measuring and correcting for the background

For all these measurements, we characterized the magnetic background by measuring a few points with the magnet holders removed and assumed the field to be linear. We would fit[2] a first order polynomial

$$B_{bkg}(z) \approx az + b. \tag{5.1}$$

to the data to approximate the background $B_{bkg}(z)$. Subtracting the background from the magnetic field then yields the magnetic field generated by the permanent magnets as

$$B_{mag}(z) = B_{meas}(z) - B_{bkg}(z). \tag{5.2}$$

Uncertainties could then be calculated using error propagation.

[2]The fit was done using a non-linear least squares method, via the *curve_fit* function in the Python package *scipy.optimize*. We used scipy version 0.19.1.

5.2 Axial magnetic field characterization

The axial characterization was done for a Helmholtz-like configuration with a separation of $\Delta = (25.0 \pm 0.2)$ cm and for two non-Helmholtz-like configurations with $\Delta = (20 \pm 1)$ cm and $\Delta = (33 \pm 1)$ cm.

5.2.1 Helmholtz-like configuration

The results of the axial characterization when the magnet holder separation was in a Helmholtz-like configuration with $\Delta = (25.0 \pm 0.2)$ cm is shown in figure 5.4. To compare this to what we would expect from a Helmholtz-like configuration, we can consider equation (3.12). In the Helmholtz-like configuration, all non-constant terms lower then the 4:th order cancel. Therefore we also show a fit to a 4:th degree polynomial

$$B(z) \approx B_0 + B_4(z - z_0)^4 \tag{5.3}$$

where B_0 is the magnetic field at $z = 0$, B_4 is the coefficient of the 4:th order term and z_0 is the center position. From the fit we get $B_0 = (3.125 \pm 0.002)$ G, which can be compared to the 3.2 G predicted by theory. Do note that the uncertainty of 0.002 G comes from the fit. There is also an additional uncertainty of 0.1 G imposed by the resolution of the Hall probe.

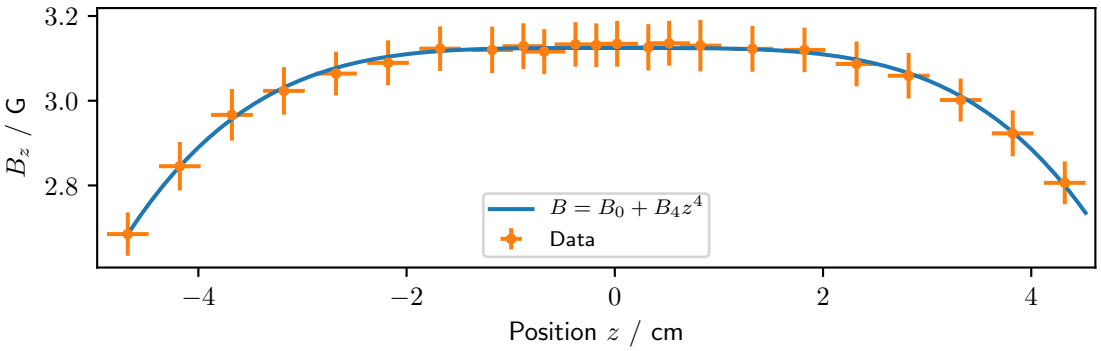

Figure 5.4: Axial magnetic field strength B_z between the magnet holders.

The measured magnetic field strengths in figure 5.4 seems to be in reasonable agreement with what we would expect. Any deviations fall within one error bar. The uncertainty here is limited by the Hall probe resolution of 0.1 G.

5.2.2 Non-Helmholtz-like separations

The results of the measurements with separations $\Delta = (20 \pm 1)$ cm and $\Delta = (33 \pm 1)$ cm are shown in figure 5.5, together with a fit of equation (3.11) to com-

pare the results to predictions from theory.

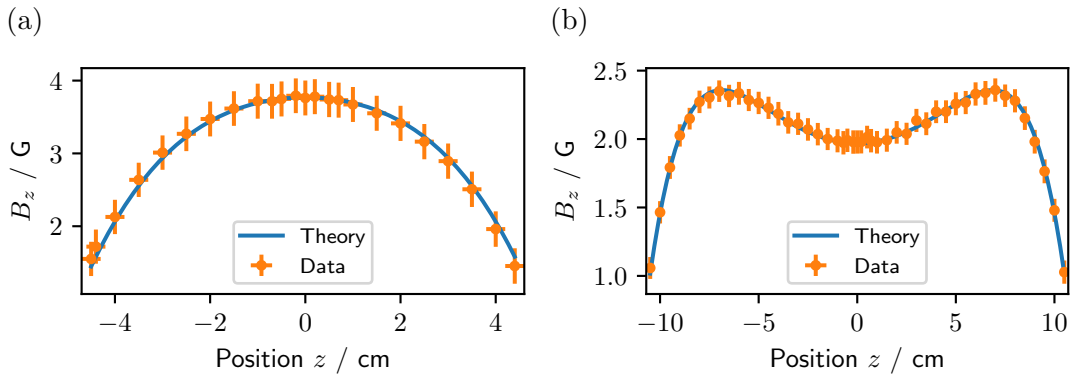

Figure 5.5: The magnetic field strength B_z when (a) the holder separation $\Delta = (20 \pm 1)\,\text{cm}$ is too small or (b) too large, $\Delta = (33 \pm 1)\,\text{cm}$, for a Helmholtz-like configuration, $\Delta = \Delta_+ = 25\,\text{cm}$.

In particular we would rewrite equation (3.11) using a center position z_0 and a scaling factor P to

$$B_z = P\left[\frac{1}{r_L^3}\left(\frac{3(z - z_0 + \Delta/2)^2}{r_L^2} - 1\right) + \frac{1}{r_R^3}\left(\frac{3(z - z_0 - \Delta/2)^2}{r_R^2} - 1\right)\right]. \tag{5.4}$$

Here $r_L = \sqrt{(z - z_0 + \Delta/2)^2 + R^2}$ and $r_R = \sqrt{(z - z_0 - \Delta/2)^2 + R^2}$. The fitting parameters were z_0, P and Δ. The radial position R of the magnets was kept at 73.8 mm. By comparing P with equations (3.2) and (3.11) we can estimate the remanence as

$$B_r = \frac{8\pi P}{VN} \tag{5.5}$$

where V is the volume of the magnets and $N = 160$ the total number of magnets.

From figure 5.5 we can see that the measured magnetic field strengths seems to be in excellent agreement with what is expected from theory. For the smaller separation we obtained from the fit that $\Delta_{small} = (19.76 \pm 0.02)\,\text{cm}$, while from the fit for the larger separation we got $\Delta_{large} = (32.67 \pm 0.02)\,\text{cm}$. These are close to the measured separations. Using equation (5.5) we got a remanence of $B_{r,small} = (0.7954 \pm 0.0009)\,\text{T}$ and $B_{r,large} = (0.7917 \pm 0.0012)\,\text{T}$ for the smaller and larger separation, respectively. The uncertainty came from the fit. These values for B_r are smaller then the $B_r \geq 1\,\text{T}$ provided by the company.

5.3 Transverse characterization

The transverse characterization was done with the magnet holders in Helmholtz-like configuration, separated by $\Delta = (25.0 \pm 0.2)\,\text{cm}$. The results are shown in figure 5.6, for each of the magnetic field components. As before we moved the Hall probe along the x-axis, but over a larger region this time.

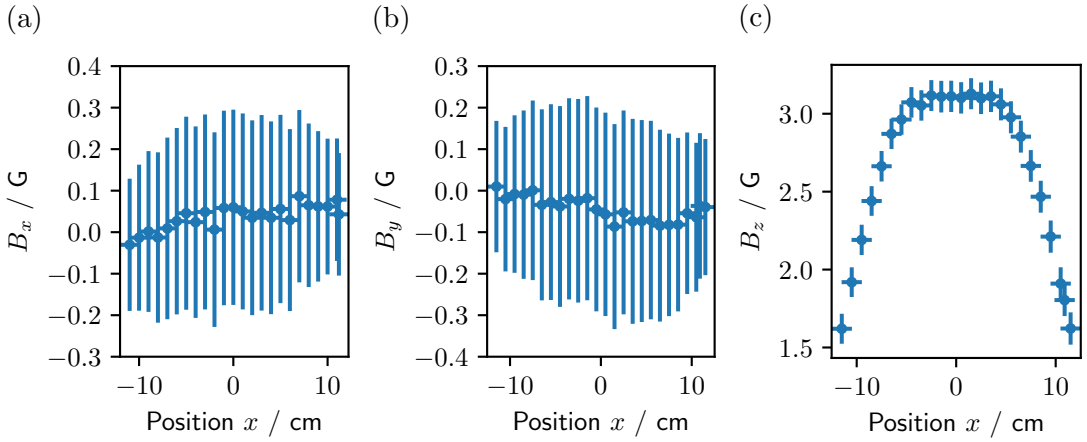

Figure 5.6: The (a) x-, (b) y- and (c) z- components of the magnetic field when moving the Hall probe along the x-axis.

For figures 5.6(a) and 5.6(b), if aligned properly we would expect these to be evenly distributed around 0 G in magnetic field, but we do see a gradient. However, for all values of B_x and B_y, 0 G lies within the error bars. The resolution of the Hall probe as well as an uncertainty $\Delta\theta$ in the Hall probe angle are the limiting factors here. In figure 5.6(c) we can see something similar to the axial measurements in section 5.2. B_z is remarkably flat around $x = 0$.

As mentioned above, a source of uncertainty was the angle of the Hall probe. While great care was taken to ensure the Hall probe measured the right component, it could still be at a small angle. Additionally, since B_y and B_z was measured before the respective backgrounds, the angle could have changed when the background was measured. We estimate that this might introduce an uncertainty of $\Delta\theta \approx 4°$ against the desired direction. Since B_x and B_y are small compared to B_z, we can estimate the added uncertainty of $B_z \sin(\Delta\theta)$. For B_z the uncertainty introduced by $\Delta\theta$ is small.

One source of uncertainty is that the Hall probe might not be perfectly aligned with the x-, y- and z-axes. This could be an issue if the misalignments were large, but due to how flat 5.6(c) is this is not likely the case.

Chapter 6

Characterizing the magnetic field with an ion

In this chapter we describe the installation of the magnet holders. We also characterize the magnetic field using the ion and present the results.

6.1 Installation of permanent magnets around the ion trap

To install the permanent magnets we replaced the coils with the magnet holders. Due to the magnet holder design, it was possible to mount them on the vacuum chamber without changing the mounting. Using washers and nuts as padding we made sure the magnet holder separation was $\approx 25\,\mathrm{cm}$, to get a Helmholtz-like configuration. One of the installed magnet holders is shown in figure 6.1.

Initial measurements of the magnetic field strength using the ion gave us a magnetic field strength of $B \approx 4.4\,\mathrm{G}$. This was $\approx 1\,\mathrm{G}$ too large and is likely the result of external magnetic field not taken into account by the calculations. To solve this 20 magnets were removed so we used 60 instead of 80 magnets per magnet holder. After this we measured $B \approx 3.46\,\mathrm{G}$.

6.2 Measurements

The magnetic field was measured by spectroscopy of different Zeeman transitions, while the magnetic field fluctuations were measured using qubit coherence.

To characterize the effects of the magnet holders, we carried out Ramsey measurements for both the coils and the magnet holders. Two transitions between

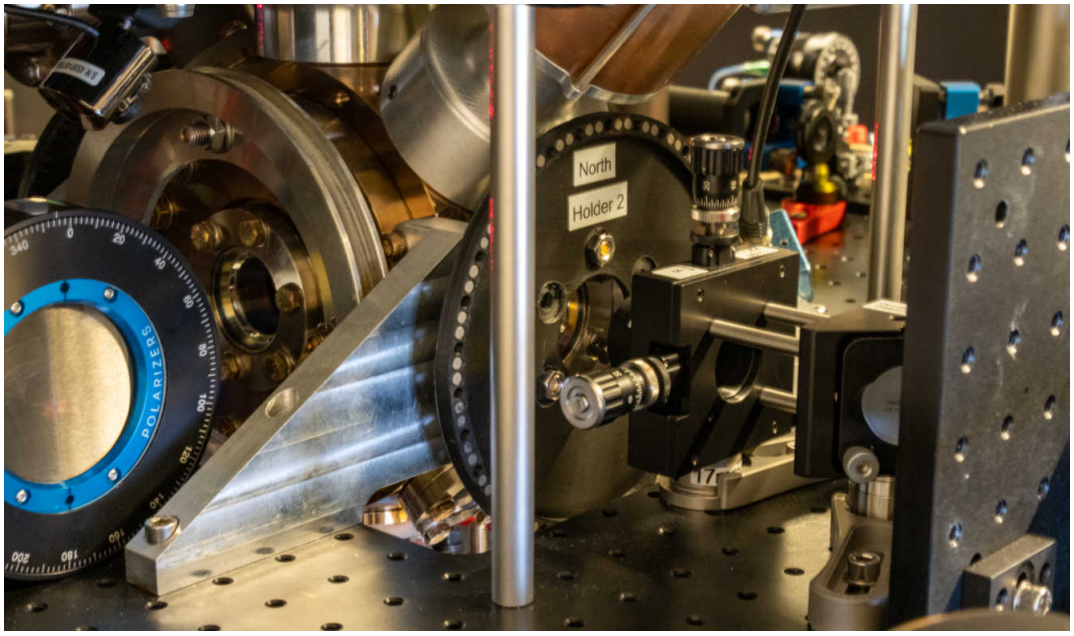

Figure 6.1: Picture of one of the installed magnet holders. It is mounted on the side of the vacuum vessel containing the ion trap and has 60 magnets inserted.

Zeeman sublevels of $5S_{1/2}$ and $4D_{5/2}$ were used in these measurements. One sensitive to magnetic fields and one relatively insensitive.

$$\text{Sensitive: } 5S_{1/2}(m_j = -1/2) \leftrightarrow 4D_{5/2}(m_j = -5/2),$$
$$\text{Insensitive: } 5S_{1/2}(m_j = -1/2) \leftrightarrow 4D_{5/2}(m_j = -1/2).$$

The transition to $4D_{5/2}(m_j = -5/2)$ is more sensitive to magnetic field fluctuations then the transition to $4D_{5/2}(m_j = -1/2)$. This can be seen by considering the energy shift ΔE of the levels due to the Zeeman effect. In particular, in an external magnetic field B it can be shown that $\Delta E = \Delta\mu B$, where $\Delta\mu$ is the sensitivity of the transition to magnetic fields. From the Zeeman effect we can get $\Delta\mu$ as

$$\Delta\mu = (g_D m_{j,D} - g_S m_{j,S})\,\mu_B \tag{6.1}$$

where $g_S \approx 2$ and $g_D \approx 6/5$ are the Landé g-factors of the $5S_{1/2}$ and $4D_{5(2}$ levels and $m_{j,S}$ and $m_{j,D}$ are the magnetic quantum numbers. μ_B is the Bohr magneton. Thus for the sensitive and insensitive transition we can calculate $\Delta\mu_{sens}$ and $\Delta\mu_{insens}$

$$\frac{\Delta\mu_{sens}}{h} \approx -2.80 \text{ MHz/G}, \tag{6.2}$$
$$\frac{\Delta\mu_{insens}}{h} \approx 0.56 \text{ MHz/G}. \tag{6.3}$$

We can see that the sensitive transition is shifted by a factor of 5 more then the insensitive transition, and thus is affected more by fluctuations.

From equations (6.2) and (6.3) we can also see that the magnetic field gradient is important, since a gradient means ions at different positions in the ion trap will have their transitions shifted relative to each other. To characterize the magnetic field gradient we measured the magnetic field strength using the ion at different positions along the trap axis. The magnetic field strength was determined by measuring the difference in resonance frequencies of the two Zeeman transitions. Their frequency difference is due to the Zeeman effect and can thus be used to calculate the magnetic field.

These measurements were done using the coils, before installing the permanent magnets, as well as using the permanent magnets. We also did this both with and without the compensation coils active. The measurements were synchronized to the 50 Hz mains using a line trigger to improve coherence. Some measurements were repeated without the line trigger to see its effect, but unless stated otherwise the line trigger was on for the presented results.

6.2.1 Ramsey measurements

To measure coherence times, we performed Ramsey measurements [15] on the ion. These consist of two resonant $\pi/2$-pulses of the 674 nm qubit laser separated by a wait time t_{wait}. These pulses couple the Zeeman sub-levels of $5S_{1/2}$ and $4D_{5/2}$ on either the sensitive or insensitive transition, used as the qubit states $|1\rangle$ and $|0\rangle$. This is illustrated in figure 6.2.

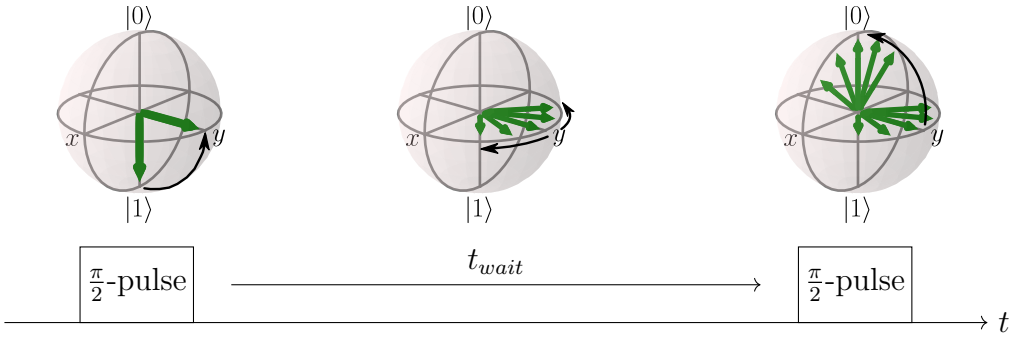

Figure 6.2: Pulse sequences in a Ramsey experiment with wait time t_{wait} and its effects on the Bloch vector. The first $\pi/2$-pulse rotates the Bloch vector from $|1\rangle$ to the equator. During the wait time noise fluctuations introduce a random phase causing the Bloch vector to rotate around the equator. The second $\pi/2$-pulse then rotates the Bloch vector up to $|0\rangle$ in the case of no noise, and close to $|0\rangle$ if noise is present. This is the case for when the second $\pi/2$-pulse is in phase with the first.

At the start of the Ramsey experiment the ion is prepared in the state $|1\rangle$. A $\pi/2$-pulse is then applied, rotating the Bloch vector to the equator and thus placing the ion in the superposition state $(|0\rangle + |1\rangle)/\sqrt{2}$. The phase of the laser field defines the axis of rotation, and by convention this will be the x-axis. The ion is then left alone for a wait time t_{wait}, during which the laser intensity on the ion is switched off[1] and the state is free to evolve. Any noise or detuning from resonance causes the Bloch vector to rotate and the qubit picks up a phase ϕ so its state becomes $(|0\rangle + e^{i\phi}|1\rangle)/\sqrt{2}$. The Bloch vector will thus rotate around the equator in the Bloch sphere. A second $\pi/2$-pulse is then applied, with a relative phase $\Delta\varphi$ to the first. $\Delta\varphi$ determines the rotation axis of the second pulse in the equatorial plane, which will be at an angle $\Delta\varphi$ to the first rotation axis. After the second $\pi/2$ pulse the final state is determined as described in section 6.2.2. By repeating this many times, 100 times in the experiment, we can estimate the population in $4D_{5/2}$. With noise ϕ may differ randomly between each measurement, giving us an uncertainty in the final state. The longer the wait time, the more phase ϕ accumulates and thus the result of each measurement may fluctuate. Fluctuations in $\Delta\varphi$ have the same effect.

By scanning $\Delta\varphi$ from 0 to 2π the population in $4D_{5/2}$ is observed to oscillate from 1 to 0 and then back up to 1 again, corresponding to oscillations between $|1\rangle$ and $|0\rangle$. The contrast[2] of these oscillations will be 1 if we have no decoherence mechanisms. Of course, in physical systems we will have noise and thus decoherence, which means that for longer wait times the qubit starts to decay from a coherent superposition state into a mixed state. This is due to fluctuations in ϕ. If ϕ fluctuates between each measurement then the final Bloch vector fluctuates as well. So after scanning $\Delta\varphi$ we would not get the expected contrast of 1, since these Bloch vector fluctuations average to result to a lower contrast. Effectively this reduces the length of the Bloch vector to less then 1. As such, to quantify the coherence time, we repeat the measurements above for many wait times and characterize the contrast decay.

The shape of this contrast decay depends on the nature of the noise responsible for the decoherence. For white noise the contrast decay is exponential, but it can have, for example, Gaussian characteristics as well, as in [15]. Gaussian characteristics, according to section 6.3, occur due to temporal correlation in the noise.

[1] This is done by using an Acousto-Optical Modulator (AOM) to stop the laser light from going to the ion.

[2] Here contrast means that difference between the maximum and minimum values.

6.2.2 Measuring the population with electron shelving

The population in $4D_{5/2}$ is determined via the *electron shelving technique* [16][5] illustrated in figure 6.3. The $5S_{1/2} \leftrightarrow 5P_{1/2}$ transition is driven using a 422 nm laser. If the ion is in the $5S_{1/2}$ state then it will scatter photons and we see fluorescence, which is detected via a photomultiplier tube (PMT). But if it is in the $4D_{5/2}$ state then it will not scatter photons and the ion will appear dark. This way we can determine if the ion is in the $4D_{5/2}$ state or not by simply looking at its fluorescence. Repeating an entire experimental sequence many times allows determination of the population in $4D_{5/2}$.

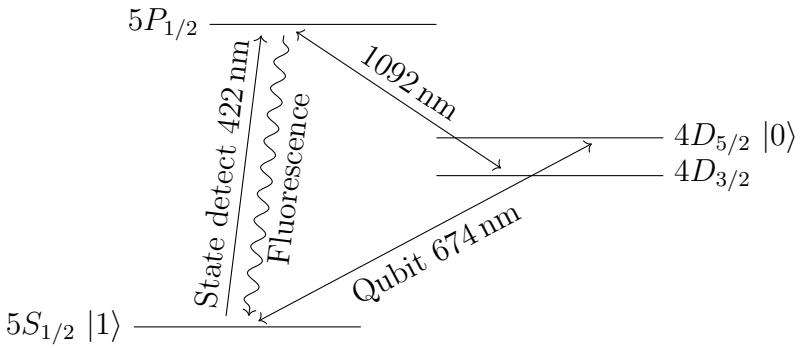

Figure 6.3: The relevant energy levels for state detection. The $5S_{1/2} \leftrightarrow 5P_{1/2}$ transition is driven with a 422 nm laser. If the ion is in state $5S_{1/2}$ the ion will appear bright, but if it is in state $4D_{5/2}$ it will appear dark.

Since there is a finite probability that the $5P_{1/2}$ state will decay to the $4D_{3/2}$ state, a 1092 nm repumping laser driving the $4D_{3/2} \leftrightarrow 5P_{1/2}$ transition is used to bring back population to $5P_{1/2}$, from which it may decay to $5S_{1/2}$. If this was not done it would be possible for a $5S_{1/2}$ state to be seen as dark, and then we would mistake it for the $4D_{5/2}$ state.

6.3 Noise model and coherence times

To quantify the coherence times for the Ramsey and spin-echo measurements, we fit a Gaussian $Ae^{-t^2/2\tau^2}$ to the contrast decay. Here A is the initial contrast and τ is the coherence time, which are used as free parameters for the fits. As a consequence the coherence time is defined as when the contrast has decayed to $1/\sqrt{e}$ of its initial amplitude.

To motivate this type of fit, we can follow the treatment in [17][7] but[3] deriving

[3]Also we only consider 1 qubit where the papers are more generic and model a N-qubit system

coherence times instead of fidelity. There the phase noise affecting a qubit is modeled as

$$\hat{H}_{noise}(t) = \frac{\Delta E(t)\hat{\sigma}_z}{2} \tag{6.4}$$

where $\Delta E(t)$ is the energy fluctuation as a function of time and $\hat{\sigma}_z$ represents how the phase fluctuation acts on the qubit as a rotation around the z-axis of the Bloch sphere. For magnetic field fluctuations we have that $\Delta E(t) = \Delta\mu\Delta B(t)$, where $\Delta\mu$ is the magnetic sensitivity of the transition, while laser phase noise[4] can be modeled as a fluctuating frequency detuning $\Delta\omega(t)$ giving us $\Delta E(t) = \hbar\Delta\omega(t)$.

Using this Hamiltonian we can calculate the time evolution of the state $|\psi\rangle$ due to the influence of the noise as

$$|\psi(t)\rangle = \exp\left(-\frac{i}{\hbar}\int_0^t dt'\,\hat{H}_{noise}(t')\right)|\psi(0)\rangle \tag{6.5}$$

where the exponential is the time evolution operator. In a Ramsey experiment the first $\pi/2$-pulse prepares the initial state $|\psi(0)\rangle = (|0\rangle + |1\rangle)/\sqrt{2}$. $\hat{H}_{noise}(t)$ causes an accumulation of random phase due to $\Delta E(t)$ and we get

$$|\psi(t)\rangle = \frac{1}{\sqrt{2}}\left(\exp(-i\phi)|0\rangle + \exp(i\phi)|1\rangle\right). \tag{6.6}$$

where

$$\phi = \frac{1}{2\hbar}\int_0^t dt'\Delta E(t'). \tag{6.7}$$

For many repetitions of the Ramsey experiment we describe the ensemble of the states with the density operator $\hat{\rho}(t)$. The off-diagonal elements of $\hat{\rho}$ are related to the coherence of the system. In particular, $\hat{\rho}$ averaged over the fluctuations $\Delta E(t)$ can be expressed as

$$\hat{\rho}(t) = \overline{|\psi(t)\rangle\langle\psi(t)|} = \frac{1}{2}\sum_{j,k=0,1}\overline{\exp\left[(-1)^{j+1}i\phi\right]|j\rangle\langle k|\exp\left[(-1)^{k+1}i\phi\right]^\dagger}. \tag{6.8}$$

with the bar $\overline{Q}$ denotes the ensemble average of some quantity Q. This can be more conveniently be expressed in matrix form. If we define the coefficients of $|0\rangle$ and $|1\rangle$ to be $c_0 = \exp(-i\phi)/\sqrt{2}$ and $c_1 = \exp(i\phi)/\sqrt{2}$, then

$$\hat{\rho}(t) = \frac{1}{2}\begin{pmatrix}1 & 2\overline{c_0c_1^*}\\ 2\overline{c_1c_0^*} & 1\end{pmatrix} = \begin{pmatrix}\rho_{11} & \rho_{12}\\ \rho_{21} & \rho_{22}\end{pmatrix}. \tag{6.9}$$

subject to a collective phase noise instead.

[4]The laser is not illuminating the ion during the wait time, but it is on and fluctuates which affects the relative phase between the first and second $\pi/2$ pulse.

We can now calculate the coherence [2][11] $C(t) = 2|\rho_{12}|$. To evaluate this, first consider the term corresponding to ρ_{12} in $\hat{\rho}$, which we will denote $\hat{\rho}_{12}$. We get

$$\hat{\rho}_{12} = \frac{1}{2}\overline{\exp\left(-2i\phi\right)}|0\rangle\langle 1| \tag{6.10}$$

If we now assume that $\Delta E(t)$ is Gaussian distributed for each time t, i.e. that we have a Gaussian process, we can use the Gaussian moment theorem[18] to show that[5]

$$\overline{\exp(-2i\phi)} = \exp\left(-2\overline{\phi^2}\right) \tag{6.11}$$

then $\hat{\rho}_{12}$ becomes

$$\hat{\rho}_{12} = \frac{1}{2}\exp\left(-2\overline{\phi^2}\right)|0\rangle\langle 1|. \tag{6.12}$$

And thus we have found that $\rho_{12} = \exp\left(-2\overline{\phi^2}\right)/2$, giving us $C(t)$ as

$$C(t) = 2|\rho_{12}| = \exp\left(-2\overline{\phi^2}\right). \tag{6.13}$$

By considering the definition of ϕ we can see that

$$\exp\left(-2\overline{\phi^2}\right) = \exp\left(-\frac{1}{2\hbar^2}\int_0^t dt_1 \int_0^t dt_2\, \overline{\Delta E(t_1)\Delta E(t_2)}\right) \tag{6.14}$$

Now we assume that the noise is a stationary process, meaning that the correlation is independent of any time shift. In other words for all time shifts t_{shift}

$$\overline{\Delta E(T + t_{shift})\Delta E(t_{shift})} = \overline{\Delta E(T)\Delta E(0)}. \tag{6.15}$$

If we use this and make a change of variables to $T = t_1 - t_2$ and $t' = (t_1 + t_2)/2$, we get

$$\exp\left(-2\overline{\phi^2}\right) = \exp\left(-\frac{1}{2\hbar^2}\int_0^t dT\,(t - T)\overline{\Delta E(T)\Delta E(0)}\right) \tag{6.16}$$

If we now assume that the correlation exhibits an exponential decay with decay rate γ

$$\overline{\Delta E(T)\Delta E(0)} = \overline{\Delta E^2}e^{-\gamma T} \tag{6.17}$$

then we can solve the integral to obtain

$$\begin{aligned} C(t) &= \exp\left(-\frac{1}{2\hbar^2}\int_0^t dT\,(t - T)\overline{\Delta E^2}e^{-\gamma T}\right) = \\ &= \exp\left(-\frac{\overline{\Delta E^2}}{\hbar^2\gamma^2}\left[e^{-\gamma t} + \gamma t - 1\right]\right) = \\ &= \exp\left(-\frac{1}{T_2\gamma}\left[e^{-\gamma t} + \gamma t - 1\right]\right) \end{aligned} \tag{6.18}$$

[5]Equation (6.11) is derived in appendix B.

where in the last step defined $T_2 = \hbar^2\gamma/\overline{\Delta E^2}$. Now let us consider the two limiting cases when γt is large and small.

In the limit where $\gamma t \gg 1$ the coherence exponentially decays as $C(t) \approx e^{-t/T_2}$, this is known as the Markovian limit. This unfortunately does not give a very good fit to our data.

In the limit where $\gamma t \ll 1$ we obtain the Gaussian decay $C(t) \approx e^{-t^2/2\tau^2}$, where $\tau = \sqrt{T_2/\gamma}$. In other words, as long as t is smaller then the characteristic time $1/\gamma$ for the correlation $\overline{\Delta E(t)\Delta E(0)}$ to decay to $1/e$ the coherence decays approximately as a Gaussian. This does give a good fit for our data.

6.3.1 Analyzing noise using coherence time measurements

We now assume to have two noise sources, namely magnetic field fluctuations $\Delta E_B(t)$ and laser frequency fluctuations $\Delta E_L(t)$. Furthermore we assume that $\Delta E_B(t)$ is not correlated to $\Delta E_L(t)$ and that both of them individually satisfy equation (6.17). With $\Delta E(t) = \Delta E_B(t) + \Delta E_L(t)$, we can then calculate the coherence

$$C(t) = \exp\left(-\frac{1}{\hbar^2}\sum_{k=B,L}\frac{\overline{\Delta E_k^2}}{\gamma_k^2}\left[e^{-\gamma_k t} + \gamma_k t - 1\right]\right) \tag{6.19}$$

where γ_B and γ_L are the decay rates for the correlations $\overline{\Delta E_B(t)\Delta E_B(0)}$ and $\overline{\Delta E_L(t)\Delta E_L(0)}$, respectively. The two noise sources add quadratically in the coherence. Note that since we have opted to write $C(t)$ in terms of $\overline{\Delta E_L^2}$ and $\overline{\Delta E_B^2}$ rather then with T_2 times, since these are the quantities of interest here.

If we now assume fast correlation decays, so $\gamma_B t \ll 1$ and $\gamma_L t \ll 1$, we can perform a Taylor expansion of the $e^{-\gamma_k t}$ term to second order

$$e^{-\gamma_k t} \approx 1 - \gamma_k t + \frac{(\gamma_k t)^2}{2}. \tag{6.20}$$

where higher order terms have been neglected since $\gamma_k t \ll 1$. Combining this with equation (6.19) yields after some simplification

$$C(t) = \exp\left(-\frac{\overline{\Delta E_B^2} + \overline{\Delta E_L^2}}{2\hbar^2}t^2\right). \tag{6.21}$$

Defining $\tau = \hbar/\sqrt{\overline{\Delta E_B^2} + \overline{\Delta E_L^2}}$ allows us to once again express this as

$$C(t) = \exp\left(-\frac{t^2}{2\tau^2}\right). \tag{6.22}$$

Now let us relate $\Delta E_B(t)$ and $\Delta E_L(t)$ to the magnetic field and laser frequency fluctuations $\Delta B(t)$ and $\Delta\omega(t)$. For the laser frequency fluctuations this relationship is $\Delta E_L(t) = \hbar\Delta\omega(t)$. For the magnetic field, we first need to consider the Zeeman energy shift of the transitions due to external magnetic fields. In case of $5S_{1/2}(m_j = -1/2) \leftrightarrow 4D_{5/2}(m_{j,D})$ transitions, we calculate a shift of $(1 + 6m_{j,D}/5)\mu_B B_{ext}$ in an external magnetic field B_{ext}. As such $\Delta E_B(t) = \Delta\mu\Delta B(t)$, where $\Delta\mu$ is the magnetic sensitivity defined in equation (6.1). The coherence time τ can now expressed in terms of the magnetic field and laser frequency fluctuations as

$$\tau = \frac{\hbar}{\sqrt{\Delta\mu^2\overline{\Delta B^2} + \hbar^2\overline{\Delta\omega^2}}}. \tag{6.23}$$

We probe two transitions which we denote a and b, with the corresponding magnetic field sensitivities $\Delta\mu_a$ and $\Delta\mu_b$. From this we determine the coherence times of the transitions to be τ_a and τ_b. We obtain two equations

$$\tau_a = \frac{\hbar}{\sqrt{\Delta\mu_a^2\overline{\Delta B^2} + \hbar^2\overline{\Delta\omega^2}}}, \tag{6.24}$$

$$\tau_b = \frac{\hbar}{\sqrt{\Delta\mu_b^2\overline{\Delta B^2} + \hbar^2\overline{\Delta\omega^2}}}. \tag{6.25}$$

Assuming the difference in coherence time is due to the different magnetic field sensitivities of the two transitions, this allows us to deduce $\overline{\Delta B^2}$ and $\overline{\Delta\omega^2}$. After some algebra we can get that

$$\overline{\Delta B^2} = \frac{\hbar^2}{\Delta\mu_b^2 - \Delta\mu_a^2}\left(\frac{1}{\tau_b^2} - \frac{1}{\tau_a^2}\right), \tag{6.26}$$

$$\begin{aligned}\overline{\Delta\omega^2} &= \frac{1}{\tau_a^2} + \frac{1}{1 - (\Delta\mu_b/\Delta\mu_a)^2}\left(\frac{1}{\tau_b^2} - \frac{1}{\tau_a^2}\right) = \\ &= \frac{1}{(\Delta\mu_b/\Delta\mu_a)^2 - 1}\left(\left(\frac{\Delta\mu_b}{\Delta\mu_a}\right)^2\frac{1}{\tau_a^2} - \frac{1}{\tau_b^2}\right)\end{aligned} \tag{6.27}$$

As such, under the assumptions that the correlations decays exponentially with decay rates γ_B and γ_L, that $\gamma_B t \ll 1$ and $\gamma_L t \ll 1$ and that the difference in coherence time is due to the different sensitivity to the magnetic field of the transitions, we can infer information about $\overline{\Delta B^2}$ and $\overline{\Delta\omega^2}$ by measuring the coherence times for the two transitions.

Let transition a and b be the insensitive and sensitive transition, for which $m_{j,D} = 1/2$ and $m_{j,D} = -5/2$. According to equation (6.1) we get the magnetic sensitivities $\Delta\mu_a = 2\mu_B/5$ and $\Delta\mu_b = -10\mu_B/5$. From this and equations

(6.26) and (6.27) we can get the root mean square (RMS) of the magnetic field fluctuations and the angular frequency fluctuations

$$\sqrt{\overline{\Delta B^2}} = \frac{5\sqrt{6}\hbar}{24\mu_B}\sqrt{\frac{1}{\tau_{sens}^2} - \frac{1}{\tau_{insens}^2}}, \tag{6.28}$$

$$\sqrt{\overline{\Delta\omega^2}} = \sqrt{\frac{1}{24}\left(\frac{25}{\tau_{insens}^2} - \frac{1}{\tau_{sens}^2}\right)} \tag{6.29}$$

where $\tau_{insens} = \tau_a$ and $\tau_{sens} = \tau_b$ are the coherence times of the insensitive and sensitive transitions. Note that for $\sqrt{\overline{\Delta\omega^2}}$ to be real we must have that $\tau_{insens}/\tau_{sens} \leq 5$, with equality when $\sqrt{\overline{\Delta\omega^2}} = 0$. Conversely if we have no magnetic field noise $\sqrt{\overline{\Delta B^2}} = 0$ then $\tau_{sens} = \tau_{insens}$. This is the physically possible range for[6] τ_{insens} and τ_{sens} according to our model. Using error propagation we get the uncertainties

$$\sigma_{\sqrt{\overline{\Delta B^2}}} = \frac{5\sqrt{6}\hbar}{24\mu_B\tau_{insens}^2\tau_{sens}^2}\sqrt{\frac{\sigma_{insens}^2\tau_{sens}^6 + \sigma_{sens}^2\tau_{insens}^6}{\tau_{insens}^2 - \tau_{sens}^2}}, \tag{6.30}$$

$$\sigma_{\sqrt{\overline{\Delta\omega^2}}} = \frac{\sqrt{6}}{12\tau_{insens}^2\tau_{sens}^2}\sqrt{\frac{625\sigma_{insens}^2\tau_{sens}^6 + \sigma_{sens}^2\tau_{insens}^6}{25\tau_{sens}^2 - \tau_{insens}^2}}. \tag{6.31}$$

where σ_{insens} and σ_{sens} are the uncertainties in τ_{insens} and τ_{sens}.

We can additionally obtain a fluctuation of the transition frequency $\delta\nu$ from the magnetic field fluctuations by using the magnetic field sensitivity β, due to the Zeeman shift of a transition. $\delta\nu$ becomes

$$\delta\nu = \frac{\Delta\mu}{h}\sqrt{\overline{\Delta B^2}}. \tag{6.32}$$

6.4 Effect of a magnetic field gradient on an ion string

If there is a magnetic field gradient, transitions for the different ions in an ion string will have different frequency shifts $\Delta\nu$. For two trapped $^{88}Sr^+$ ions separated by a distance Δz in a linear magnetic field B, the sensitive and insensitive transitions will be shifted by

$$\Delta\nu = \frac{\Delta\mu}{h}\Delta z\frac{\partial B}{\partial z}. \tag{6.33}$$

[6]This can be generalized to other transitions by considering equations (6.26) and (6.27).

where $\Delta\mu$ is the magnetic field sensitivity and $\Delta z \cdot \partial B/\partial z$ is the difference in magnetic field between the ions.

Now consider an idealized scenario where the laser is resonant on one of the ions and that the only detuning on the other ion is due to the Zeeman shift. $\Delta\nu$ is then the detuning of the laser on the second ion. If the resonant Rabi frequency is Ω, the effective Rabi frequency Ω_{eff} and the amplitude A of the Rabi oscillations at the second ion are

$$\Omega_{eff} = \sqrt{\Omega^2 + (2\pi\Delta\nu)^2}, \tag{6.34}$$

$$A = \frac{\Omega}{\Omega_{eff}}. \tag{6.35}$$

The Rabi frequency in our experiment may be around 10 kHz to 100 kHz.

6.5 Experimental results

6.5.1 Ramsey measurements and coherence times

The contrast for the Ramsey measurements are shown in figure 6.4 together with the Gaussian fit of $Ae^{-t^2/2\tau^2}$. This is for both with the coils and with the permanent magnets, with and without using the compensation coils. The more and less sensitive transitions $5S_{1/2}(m_j = -1/2) \leftrightarrow 4D_{5/2}(m_j = -5/2)$ and $5S_{1/2}(m_j = -1/2) \leftrightarrow 4D_{5/2}(m_j = -1/2)$ are both shown for each case. The line trigger was active for all these measurements.

The coherence times τ for the Ramsey measurements of each case are compared in figure 6.5 for both the more and less sensitive transition. We can see that the coherence times are unfortunately not affected much by replacing the coils with permanent magnets. For the insensitive transition we can see a longer coherence time by a few hundred µs, from $\tau = (1250 \pm 50)$ µs for the coils to $\tau = (1500 \pm 80)$ µs with the magnets. For the sensitive transition the coherence time is $\tau \approx 500$ µs for both the coils and the magnets. Since the sensitive transition should see a greater improvement in coherence times it is unlikely the improvement for the insensitive transition comes from the permanent magnets. It is more likely the improvement was due to something else, perhaps even just a day to day variation.

For the $\sqrt{\overline{\Delta\omega^2}}$ obtained with the magnets coherence times seems smaller, compared to using the coils. This is likely due to day to day fluctuations. It could also be that the stabilization electronics for the coils introduced laser noise, but it is unlikely.

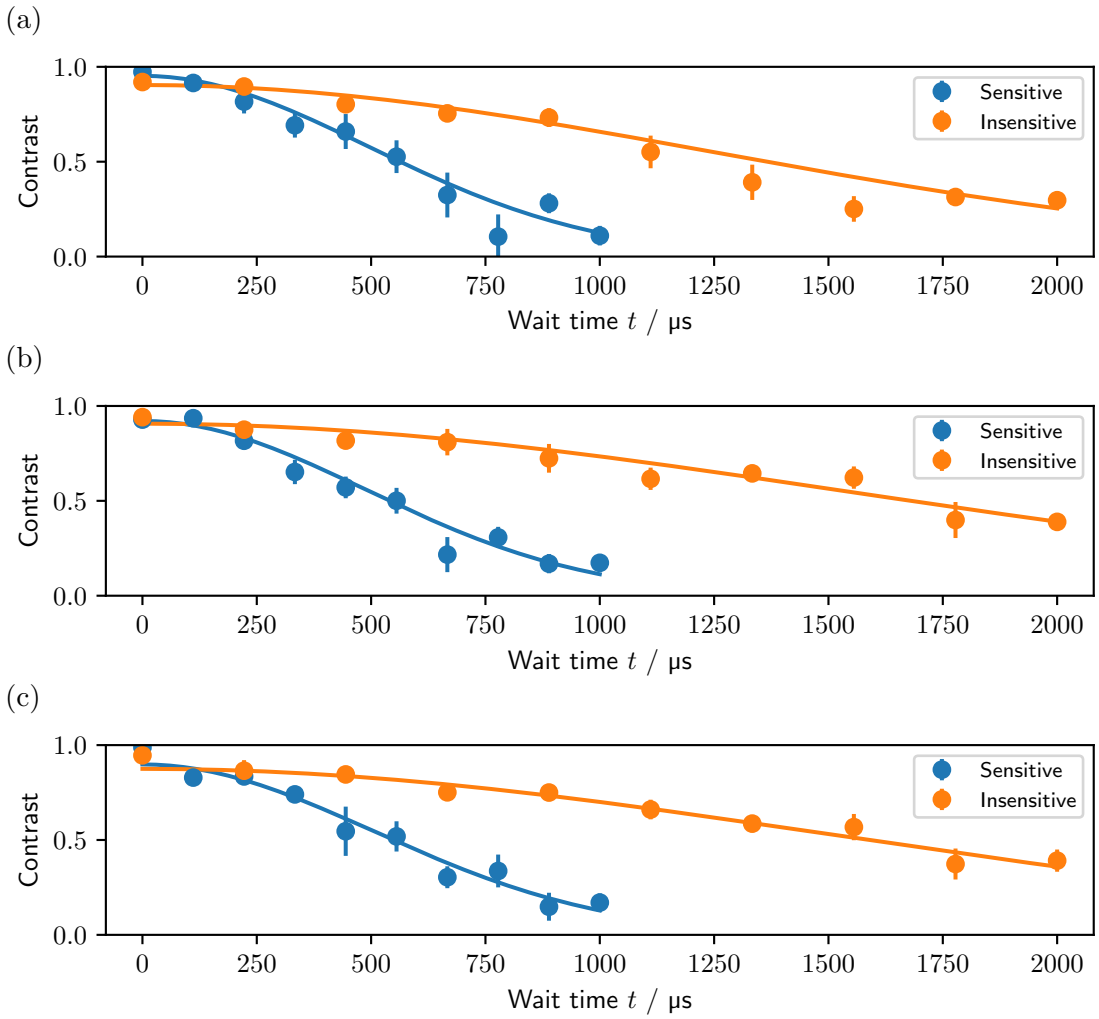

Figure 6.4: Contrast of Ramsey measurements for the more and less sensitive transitions with the line trigger, for when the coils (a) and permanent magnets with (b) and without (c) compensation coils were used. A Gaussian fit $Ae^{-t^2/2\tau^2}$ is shown for each contrast.

6.5.2 Fluctuations

Following the analysis derived in section 6.3.1, it is possible to derive some additional information about the magnetic field and laser frequency fluctuations using equations (6.28) and (6.29) as well as (6.30) and (6.31) for the uncertainty in the result. The results for when the coils and permanent magnets, with and without compensation coils, are shown in figure 6.6. From the data we get that $\sqrt{\overline{\Delta B^2}} \approx 110\,\mu\text{G}$ while $\sqrt{\overline{\Delta\omega^2}}/2\pi \approx 100\,\text{Hz}$.

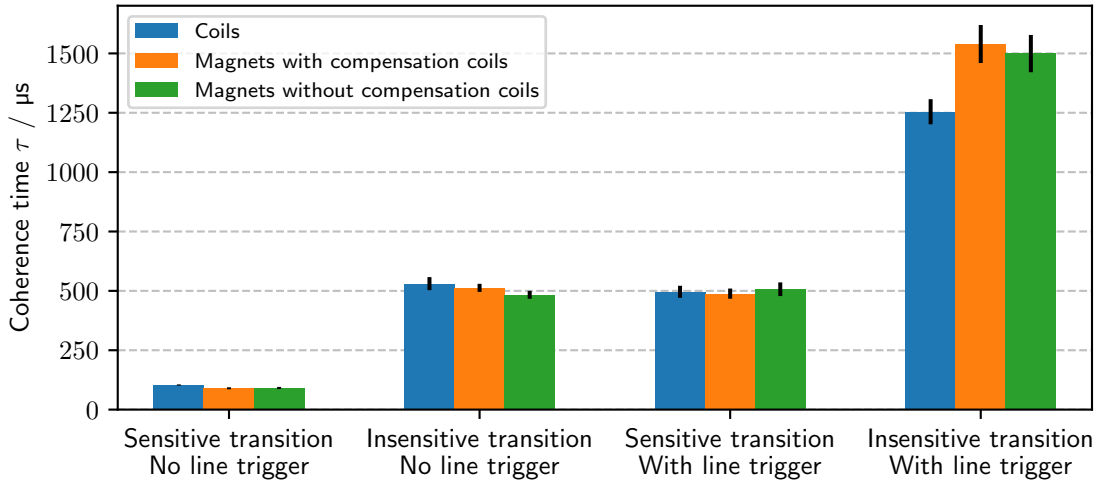

Figure 6.5: The coherence times, defined as when the contrast has decayed to $1/\sqrt{e}$, when using the coils, permanent magnets and permanent magnets without compensation coils in use. The coherence times are both for the more and the less sensitive transitions, as well as both with and without the line trigger.

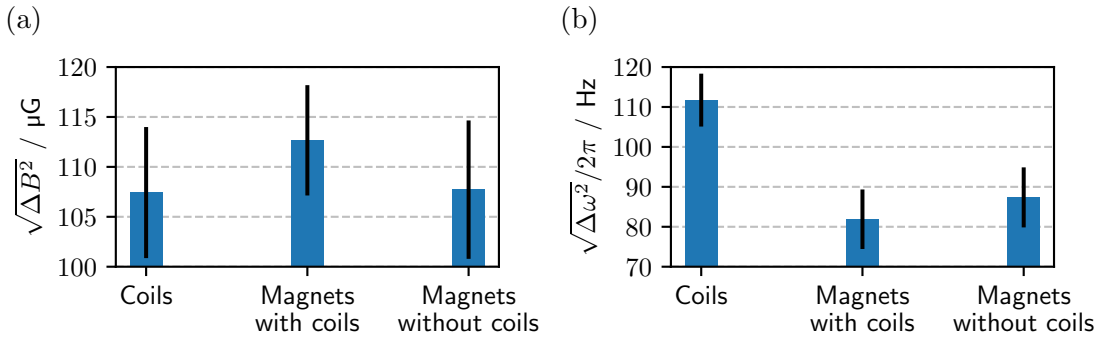

Figure 6.6: The RMS of (a) the magnetic field fluctuations and (b) laser frequency fluctuations for when the coils and magnets, both with and without the compensation coils, were used to generate the quantization magnetic field. These results were obtained as described in section 6.3.1 with the line trigger active.

We can compare $\sqrt{\overline{\Delta B^2}}$ to the results from [2], where they obtained that $\sqrt{\overline{\Delta B^2}} = 2.7{\cdot}10^{-2}$ µG. This was with a magnetic shielding and thus their magnetic field fluctuations are much lower.

To estimate the frequency fluctuations introduced via the magnetic field fluctuations we can use equation (6.32) with equations (6.3) and (6.2). Using the permanent magnets with the compensation coils the frequency fluctuations are $\delta\nu_{insens} = (63 \pm 3)$ Hz and $\delta\nu_{sens} = (-315 \pm 16)$ Hz for the insensitive and sensi-

tive transitions, respectively.

6.5.3 Measurements of the magnetic field strength

The magnetic field strength measured with the ion is shown in figure 6.7 when using the coils and the permanent magnets. The gradient for the permanent magnets has reversed direction compared to the coils, since we reversed the direction of the magnetic field when they were installed. This indicates that the magnetic field gradient is not due to the coils or magnets, but external in origin. The mean magnetic field strength measured by the ion when the coils were used was $\langle B_c \rangle = (3.545 \pm 0.002)\,\mathrm{G}$. With the permanent magnets we measured $\langle B_{m+c} \rangle = (3.457 \pm 0.002)\,\mathrm{G}$ and $\langle B_m \rangle = (3.470 \pm 0.002)\,\mathrm{G}$ with and without the compensation coils, respectively.

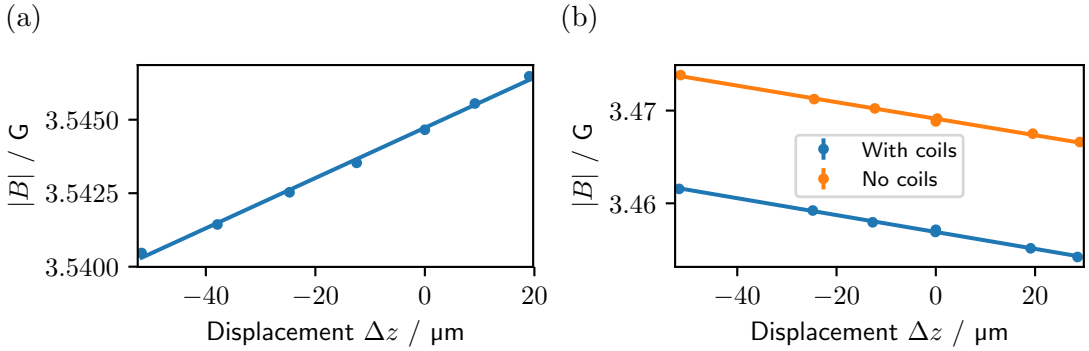

Figure 6.7: Magnetic field strength at different positions when using (a) the coils or (b) the permanent magnets to generate the magnetic field, with and without the compensation coils.

From figure 6.7 we can see that the magnetic field strength varies linearly. By fitting a first order polynomial we obtain that with the coils the magnetic field gradient at ion trap is $\partial B_c/\partial z = (85.5 \pm 1.9)\,\mu\mathrm{G}/\mu\mathrm{m}$ while the gradients with the permanent magnets are $\partial B_{m+c}/\partial z = (-91.1 \pm 2.0)\,\mu\mathrm{G}/\mu\mathrm{m}$ with the compensation coils and $\partial B_m/\partial z = (-89.1 \pm 2.5)\,\mu\mathrm{G}/\mu\mathrm{m}$ without. Assuming the magnetic field should not deviate much from the one observed in section 5.2.1, it would take a displacement of several cm from the center point to reproduce any of the $\partial B/\partial z$ presented here. Thus it is more likely the magnetic field gradient results from external magnetic fields. For example, it is possible some part of the vacuum chamber containing the ion trap has been magnetized.

Using equation (6.33) we can estimate the transition frequency shifts $\Delta\nu$ between different positions along the trap axis from these gradients. In particular, we will use $\partial B_{m+c}/\partial z$, but the other gradients should give similar results. We

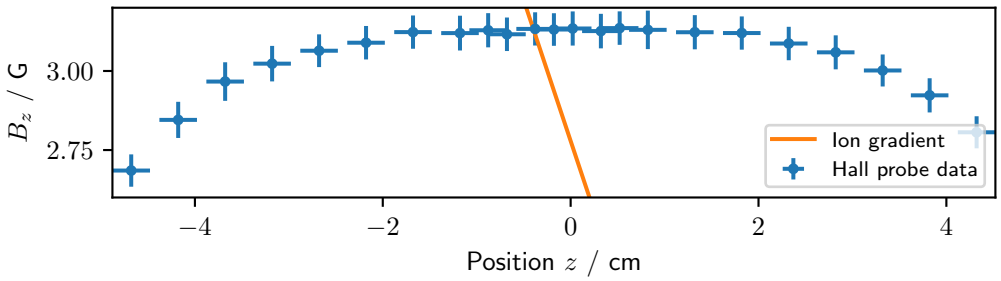

Figure 6.8: The gradient $\partial B_m/\partial z$ measured by the ion with the permanent magnets together with the magnetic field strength measured by the Hall probe in section 5.2.1, when the magnet holders were in a Helmholtz-like configuration.

can also estimate the change in effective Rabi frequency Ω_{eff} and Rabi oscillation amplitude A due to the Zeeman effect with (6.34) and (6.35). The results can be seen in figure 6.9 over 100 µm, where a resonant Rabi frequency $\Omega/2\pi = 16\,\text{kHz}$ has been assumed. This Rabi frequency has been observed in the experiment, which is why it was chosen. For the sensitive transition we can see a shift over 100 µm of $\Delta\nu = (25.5 \pm 0.6)\,\text{kHz}$, compared to a shift of $\Delta\nu = (-5.1 \pm 0.1)\,\text{kHz}$ for the insensitive transition. While Ω_{eff} increases and A decreases for both transitions, the sensitive transition is affected to a much larger degree since for it $\Omega_{eff}/2\pi = (30.1 \pm 0.5)\,\text{kHz}$ almost doubles while $A = (53.1 \pm 0.8)\,\%$ drops to almost half over 100 µm. For the insensitive transition we instead get $\Omega_{eff}/2\pi = (16.80 \pm 0.03)\,\text{kHz}$ and $A = (95.3 \pm 0.2)\,\%$. The gradient thus seems to be a problem mostly for sensitive transitions, but still has a much lower effect on insensitive transitions.

We can compare the gradients with the magnetic field strength that was measured with the Hall probe in 5.2.1. This is done in figure 6.8, where we have taken the data from figure 5.4 and then added a line representing the gradient observed by the ion. In particular, we used $\partial B_m/\partial z$ for this figure. We can see that the ion sees a much larger gradient then we would expect from the magnet holders. This indicates that the gradient is due to external magnetic fields.

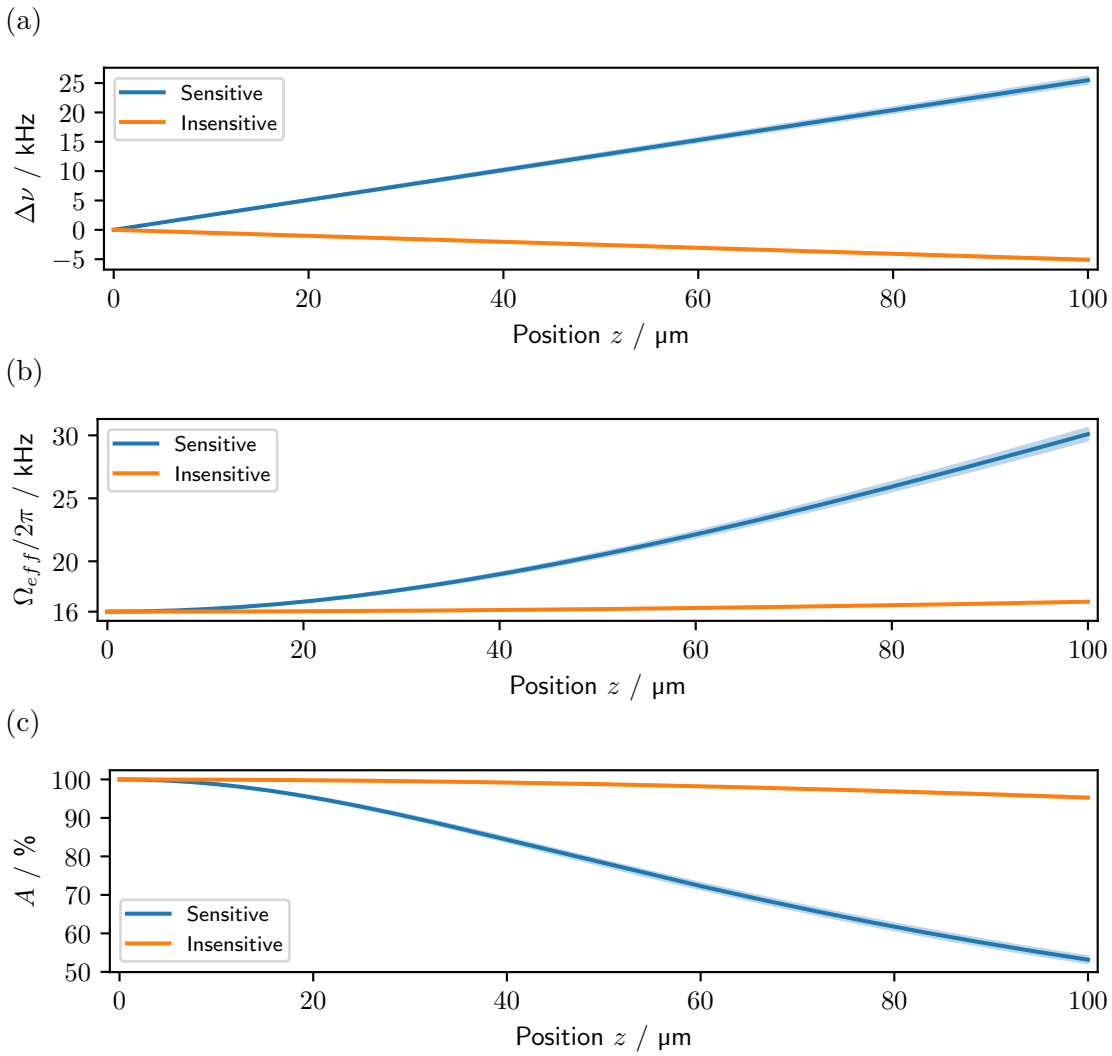

Figure 6.9: The difference in (a) transition frequency $\Delta\nu$, (b) effective Rabi frequency Ω_{eff} and (c) Rabi oscillation amplitude A along the trap axis relative to $z = 0$ due to the observed gradient in the magnetic field. This is for when the permanent magnets were used in conjunction with the compensation coils. We used a resonant Rabi frequency of $\Omega/2\pi = 16\,\mathrm{kHz}$.

Chapter 7

Discussion: Permanent magnets

This chapter contains a discussion about the permanent magnets, as well as possible further developments.

7.1 Coherence times

We did not observe an improvement in coherence time by replacing the coils with permanent magnets. This is unfortunate but not surprising, as we do not have a magnetic shield and thus fluctuations in external magnetic fields from electrical devices in the lab or even strong magnets in neighboring labs can still interact with the ions in the trap. This has been observed previously in Mainz[2], where they only observed a significant increase in coherence from the permanent magnets with a magnetic shield. It should be noted, however, that they did observe a smaller improvement to coherence without a magnetic field shielding, which we did not. It is possible we have a lot of magnetic field noise in the current setup that dominates over the fluctuations caused by the coils, and therefore we do not see an improvement. It is also possible that nearby labs, some of which has strong magnets of several tesla, could affect the results. With a magnetic shielding we should see an improvement.

7.2 Magnetic field gradient

We did observe a gradient in the magnetic field. This gradient likely is external in origin and thus generated by electrical devices in the lab, or from magnetized metal. We can draw this conclusion from the fact that the gradient was much larger then what we observed with the Hall probe in chapter 5 and since it was roughly the same with the coils as with the magnets, just with opposite direction. Through the Zeeman effect this gradient can cause shifts in the transition frequencies for

different ions in an ion string and thus in effective Rabi frequency amongst other things. This is less of an issue for transitions insensitive to the magnetic field and for higher Rabi frequencies, but it is prudent to try and reduce the gradient.

7.3 Fluctuations of magnetic field and laser frequency

In section 6.5.2 we used the theory derived in section 6.3.1 to estimate the root mean square of the magnetic field fluctuations and the laser frequency fluctuations. It seems like the magnetic field fluctuations dominate for the more sensitive transition, while being roughly equal to the laser frequency fluctuations for the less sensitive transition.

It is possible to characterize the laser linewidth using entangled or correlated states[19]. This could perhaps provide a more accurate result then the method employed here to estimate $\sqrt{\overline{\Delta\omega^2}}$.

7.4 Future developments

7.4.1 Magnetic field shielding

An important step for better coherence times is installing a magnetic shielding to isolate the ions in the ion trap from external magnetic fields from the control electronics and surrounding labs which are detrimental to the coherence times. It has been demonstrated before [2] that external magnetic field fluctuations can contribute significantly to decoherence and a magnetic shield is required to efficiently suppress these, while only replacing the coils with permanent magnets is not effective. Since the analysis of the magnetic field fluctuations in section 6.5.2 indicate that external magnetic field fluctuations contribute significantly to decoherence, shielding the ion trap from such noise will be essential.

7.4.2 Replacing the compensation coils

The compensation coils generate much weaker magnetic fields and are probably not limiting coherence times by much. Additionally with a magnetic shield they might not be needed. They are setup to generate orthogonal magnetic fields along the x- and y-axis at the ion trap and small fluctuations thus change the direction but not the magnitude to first order. Still we might want to replace the compensation coils as well with permanent magnets, to improve the magnetic field stability further.

Since the compensation coils should target specific magnetic field strengths, we likely need to adjust the number of magnets in each of the replacing magnet holders. Additionally, we probably want to use a large number of magnets to allow fine tuning the magnetic field strength. Getting the right magnetic field strength would require some effort since we cannot simply adjust the current as with the compensation coils, but it should work.

7.4.3 Compensation of the magnetic field gradient

Since the gradient appears to be due to external magnetic fields, the magnetic field shielding should help mitigate the effect and reduce the gradient. There are other alternatives to be aware of as well. The simplest way to try and reduce the gradient would be to tweak the magnet holder separation, and maybe add additional magnets to one of the holders. There are more involved possibilities as well, such as modifying the magnet holders. One could add additional rings of permanent magnets to the setup to compensate for the gradient.

7.4.4 Magnet holder improvements

The 3D printed magnets holders have so far been sufficient. That said, as has been demonstrated in figure 4.4, the 3D printer had issues creating holes and most of them would end up slightly tilted. Currently this is not known to cause a problem in the experiment. Possible solutions include tweaking the 3D printer settings and printing new magnet holders, or to manufacture magnet holders from a non-magnetic metal such as aluminium. Aluminium has been used for this application before[2] and is known to work. This would likely allow better precision when creating the holders and in particular the holes for the magnets would likely have the correct dimensions and angle.

While the Helmholtz configuration derived here has many desirable properties, it may be possible to improve upon it. As mentioned above in the discussion of the gradient, one possible improvement would be to add more rings of permanent magnets to compensate for the gradient.

7.4.5 Temperature stability of the magnetic field

Temperature stability is not currently known to be a problem, but other groups have observed [11] drifts in qubit transition frequency that have been correlated with temperature fluctuations. A solution to this problem could be active temperature stabilization with heating wires or compensation coils. Doing this would require equipment that could stabilize temperature on the appropriate level, which can be challenging.

Another approach to this problem is passive compensation using two types of magnets, such as Sm_2Co_{17} and neodymium magnets, with different temperature dependence and opposite orientations. The idea is that the temperature dependence of the two types of magnets will cancel each other, so the combined magnetic field has lower temperature dependence then either of the magnet types. This has been shown to work [11].

Chapter 8

Test setup for fiber noise cancellation

In this chapter we describe how the test setup for fiber noise cancellation was implemented. We also present the testing results.

8.1 Fiber noise

First we will describe how fibers can introduce phase noise, with a similar treatment to [20]. Consider a single mode fiber with angled end points[1] of length L, which lies in a straight line along the z-axis. We couple a monochromatic laser at frequency ω_c into this fiber at $z = 0$. This laser light is linearly polarized along the y-axis. The electric field $\vec{E}(z,t)$ in the fiber can then be written as

$$\vec{E}(z,t) = E_0 \cos(k\mathfrak{L}(z) - \omega_c t + \varphi)\hat{y} \tag{8.1}$$

where E_0 is the amplitude of the electric field, k is the wavenumber, φ is an arbitrary initial phase and $\mathfrak{L}(z)$ is the optical path length. If $n(z)$ is the refractive index at z, then

$$\mathfrak{L}(z) = \int_0^z n(s)\,\mathrm{d}s. \tag{8.2}$$

To determine how the fiber affects the light, consider the electric field $\vec{E}_{end}(t) = \vec{E}(L,t)$ at the far end of the fiber

$$\vec{E}_{end}(t) = E_0 \cos(k\mathfrak{L}(L) - \omega_c t + \varphi)\hat{y} = E_0 \cos(\omega_c t - k\mathfrak{L}(L) - \varphi)\hat{y}. \tag{8.3}$$

where we in the last step used that cos is an even function to make the $\omega_c t$ term positive. This is because that change makes things more convenient later on.

[1] For a single mode fiber, angled end points means no reflections at the end points.

The phase of $\vec{E}_{end}$ is determined by $k\mathfrak{L}(L)$, representing the phase from the propagation through the fiber, and φ, which is an initial phase. Combining these phase factors

$$\phi = -(k\mathfrak{L}(L) + \varphi) \tag{8.4}$$

allows us to write $\vec{E}_{end}(t)$ as

$$\vec{E}_{end}(t) = E_0 \cos(\omega_c t + \phi)\hat{y}. \tag{8.5}$$

Due to thermal fluctuations the fiber length L might expand or contract and if the refractive index $n(z)$ has a temperature dependence it could also change with time or position. Additionally, any vibrations the fiber picks up from its environment introduces time dependence into L. From equation (8.2) we can see that this introduces time dependence into $\mathfrak{L}(L)$ and thus into ϕ.

We can express this time dependence as $\phi(t) = m(t) + \phi_0$, where $m(t)$ contains the time dependence and ϕ_0 is a constant. This gives $\vec{E}_{end}(t)$ as

$$\vec{E}_{end}(t) = E_0 \cos(\omega_c t + m(t) + \phi_0)\hat{y}. \tag{8.6}$$

Since this modulates the instantaneous phase of the light field it is known as *phase modulation*.

The frequency of visible light lies in the hundreds of THz, which is much faster then frequency components introduced by fiber noise. It does have a detrimental affect on the frequency spectrum, though, due to spectral broadening of the laser linewidth.

It is possible to cancel fiber noise via *fiber noise cancellation* (FNC), which as been used to cancel fiber noise to sub-Hertz and even millihertz levels[9][21]. There are several approaches, but the rough idea is to back reflect some light through the fiber, use it to measure the fiber noise and then modulate the laser light going into the fiber to cancel the measured fiber noise. The setup we used is described below, in section 8.2.

8.2 Experimental setup for fiber noise cancellation

Our test setup for fiber noise cancellation is inspired by one used at ETH Zürich [20] and is illustrated schematically in figure 8.1. The optical part is shown in figure 8.2. This scheme was chosen to maximize the amount of power going to the experiment.

The laser is a Toptica TA pro extended cavity diode laser with tapered amplifier at 674 nm, with a corresponding angular frequency ω. It is used for the qubit

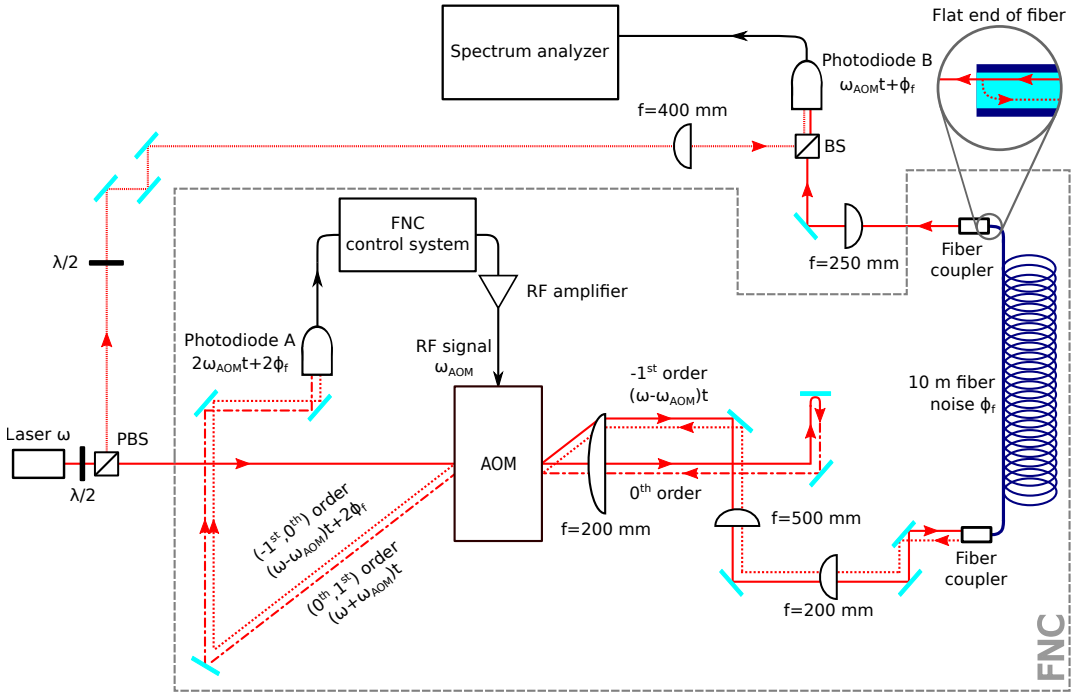

Figure 8.1: Schematic overview of the test setup for fiber noise cancellation (FNC). The control system electronics is shown in more detail in figure 8.3.

transition and has a a narrow linewidth of $\approx 100\,\text{Hz}$ as characterized in section 6.5.2. A small fraction of the laser was split off and sent to the test setup via a 10 m long fiber (not shown in figure 8.1). A $\lambda/2$-waveplate followed by a polarizing beam splitter (PBS) is then used to split off part of the laser light to photodiode B where it is overlapped with the output of the FNC setup in an out-of-loop characterization of the fiber noise. The polarization is corrected by a second $\lambda/2$-plate to match the output of the FNC setup. Most of the light, however, passes straight through the PBS to be used in the test setup as described in section 8.2.1. The first $\lambda/2$-plate was set to allow as much light as possible to pass straight to the FNC test setup.

This light passes an Acousto-Optical Modulator (AOM) driven at 100 MHz, and is then coupled into a 10 m fiber. The light from the far end of the fiber is overlapped on the (fiber coupled) photodiode B[2] with the light the was initially split off with the PBS. This creates a beat note at 100 MHz, which is then observed on a spectrum analyzer. The measures spectra are used for FNC characterization.

[2]Menlo Systems FPD 510-V.

8.2.1 Optics

The laser light that went straight through the PBS is used in the test setup for fiber noise cancellation. After the PBS it passes an AOM[3] driven at an angular frequency $\omega_{AOM}/2\pi = 100\,\text{MHz}$, which is followed by a lens with focal length $f = 200\,\text{mm}$. The 0^{th} order of the AOM is simply reflected back via two mirrors while the -1^{st} order couples into a single mode fiber[4] with a flat far end[5]. Coupling efficiency is improved with two lenses with focal lengths $f = 500\,\text{mm}$ and $f = 200\,\text{mm}$. All other AOM orders are blocked.

The back reflected 0^{th} order beam passes through the AOM a second time. The $+1^{\text{st}}$ order of this light, denoted the $(0^{\text{th}}, 1^{\text{st}})$ order, is used for the fiber noise cancellation. It has an angular frequency of $\omega + \omega_{AOM}$.

Now consider the -1^{st} order beam that couples into the fiber. In the fiber it picks up a certain phase noise ϕ_f due to vibrations or thermal fluctuations. At the far end most of the light exits the fiber and is coupled into photodiode B, but a small fraction is back reflected due to the flat end. On its way back through the fiber it picks up the same noise ϕ_f again, changing the phase by a total of $2\phi_f$. This is assuming that ϕ_f changes slowly compared to the round-trip time[6] of the light.

The back reflected laser light from the fiber passes the AOM again. The 0^{th} order beam, denoted the $(-1^{\text{st}}, 0^{\text{th}})$ order, is then used for fiber noise cancellation. It will have a frequency of $\omega - \omega_{AOM}$ and an additional phase $2\phi_f$ from passing the fiber twice. It follows the same path as the $(0^{\text{th}}, 1^{\text{st}})$ order beam.

Both the $(0^{\text{th}}, 1^{\text{st}})$ and $(-1^{\text{st}}, 0^{\text{th}})$ order beams are coupled into the fiber coupled photodiode A[7] in figure 8.1. The overlapped beams interfere and give a beat note. The total electric field is $\vec{E}_{total}(t) = \vec{E}_{-10}(t) + \vec{E}_{+01}(t)$ where

$$\vec{E}_{-10}(t) = E_{-10}\cos\left[(\omega - \omega_{AOM})t + 2\phi_f\right]\hat{\epsilon}, \tag{8.7}$$

$$\vec{E}_{+01}(t) = E_{+01}\cos\left[(\omega + \omega_{AOM})t\right]\hat{\epsilon} \tag{8.8}$$

are the electric fields for the $(-1^{\text{st}}, 0^{\text{th}})$ and $(0^{\text{th}}, 1^{\text{st}})$ order beams, respectively. $\hat{\epsilon}$ is the polarization direction and E_{-10} and E_{+01} are the electric field amplitudes.

The intensity observed by the photodiode is given by $I(t) = \epsilon_0 c\langle|\vec{E}_{tot}(t)|^2\rangle$, where $\langle|\vec{E}_{tot}(t)|^2\rangle$ is the time average of $|\vec{E}_{tot}(t)|^2$

$$|\vec{E}_{tot}(t)|^2 = |\vec{E}_{-10}|^2 + |\vec{E}_{+01}|^2 + E_{-10}E_{+01}\left(\cos\left[2\omega_{AOM}t - 2\phi_f\right] + \cos\left[2\omega t + 2\phi_f\right]\right). \tag{8.9}$$

[3] Gooch & Housego 3100-125.
[4] OZ Optics PMJ-3A3A-633-4/125-3.
[5] Normally a single mode fiber has angled ends to cancel any back reflected light.
[6] Round-trip time is the time it takes for light to enter the fiber, get reflected and then exit the fiber through the coupler it entered before.
[7] Menlo Systems FPD 510-V.

Due to the finite response time of the photodiode, it averages the optical frequency components $|\vec{E}_{-10}|^2 \to E_{-10}^2/2$, $|\vec{E}_{+01}|^2 \to E_{+01}^2/2$ and $\cos[2\omega t + 2\phi_f] \to 0$. We get $I(t)$ as

$$I(t) = I_{-10} + I_{+01} + \sqrt{I_{-10} I_{+01}} \cos(2\omega_{AOM} t - 2\phi_f) \tag{8.10}$$

where $I_{-10} = \epsilon_0 c E_{-10}^2/2$ and $I_{+01} = \epsilon_0 c E_{+01}^2/2$ are the time averaged intensities from the individual beams. The last term is not averaged out since the photodiode is fast enough to see a signal with frequency $2\omega_{AOM} = 2\pi \times 200$ MHz.

The observed beat note is amplified and filtered and then used to generate feedback in the control system, in our case a PI controller.

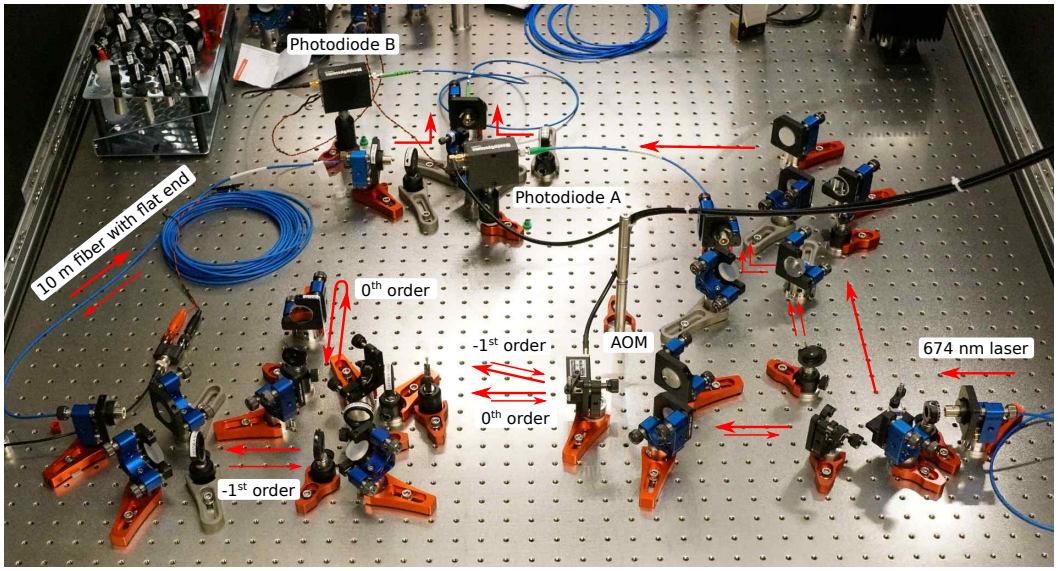

Figure 8.2: Optical part of the test setup. Note that here the laser comes from the right, rather from the left as in figure 8.1.

8.2.2 Electronics and PI controller

In broad terms, PI controller analyzes the feedback signal from the photodiode and then adjusts the driving frequency ω_{AOM} of the AOM to cancel the fiber noise ϕ_f. The setup is shown in schematically in figure 8.3, together with the model of each component. A Voltage Controlled Crystal Oscillator (VCXO), which is tunable in an ≈ 23.4 kHz range around 100 MHz, is used to drive the AOM at a frequency ω_{AOM}. From the photodiode we get a feedback signal that depends on $I(t)$ from equation (8.10), with a beat note at a frequency $\omega_{PD} = 2\omega_{AOM} \approx 2\pi \times 200$ MHz.

A bias-tee is then used to suppress DC components in the photodiode signal, after which it is amplified and filtered by two high pass filters. The high pass filters

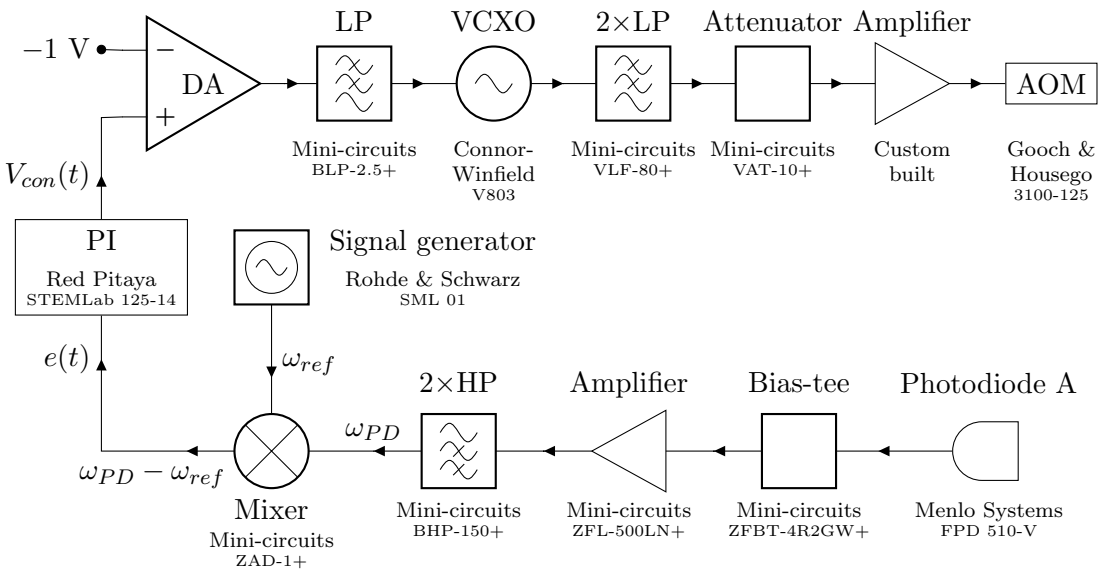

Figure 8.3: The control system, where a Red Pitaya STEMLab 125-14 is used as the PI controller. The error signal $e(t)$ comes from the photodiode and the control signal $V_{con}(t)$ adjusts the AOM through the VCXO. The differential amplifier, marked DA, is shown in figures 8.4(b) and 8.5, the latter being the schematic. Low pass filters are marked as LP or 2×LP if there are two of them. Similarly high pass filters are marked HP or 2×HP. The company and model is written under the components, except for the signal generator where it is at the side.

are used to suppress undesired lower frequency components at $\approx 100\,\mathrm{MHz}$. The signal is then mixed down to DC with a 200 MHz reference signal from a signal generator using a frequency mixer. The frequency of this mixed down signal will be the frequency difference of reference signal and the beat note, which is 0 Hz in the ideal case, but due to the phase noise from the fiber additional frequency components can be introduced. The mixed down signal is then used as an error signal $e(t)$ for the PI controller.

As a PI controller we use a Red Pitaya STEMLab 125-14, shown in figure 8.4(a). It is controlled via Ethernet using PyRPL. It uses the mixed down signal $e(t)$ as an error signal for the built in PI controller functionality, which is configured to keep $e(t)$ at 0 V.

The builtin PI controller has a proportional component P and an integrating component I, which multiplies $e(t)$ with proportionality constant as well as integrates it over time. The output control signal $V_{con}(t)$ that drives the VCXO is [22]

$$V_{con}(t) = K_p e(t) + K_i \int_0^t e(t')\,dt'. \tag{8.11}$$

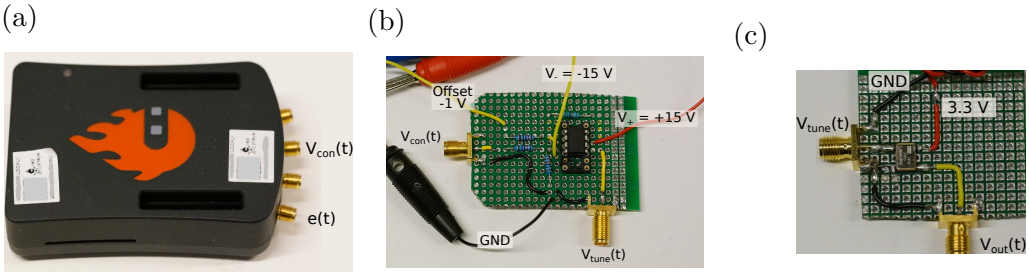

Figure 8.4: The FNC control system, consisting of (a) the Red Pitaya as a PI controller, as well as (b) the differential amplifier and (c) the VCXO. The Red Pitaya uses $e(t)$ as the error signal and outputs a control signal $V_{con}(t)$. The differential amplifier takes $V_{con}(t)$, an offset voltage of $-1\,\mathrm{V}$ and outputs a rescaled tuning voltage $V_{tune}(t)$ to the VCXO, which in turn outputs $V_{out}(t)$ which is used to drive the AOM.

where K_p and K_i are PI parameters that determine the strength of the compensation from the P and I components. The P component simply pushes the frequency in the right direction, while the I component compensates for long term drifts. We used $K_p \approx 3.1$ and $K_i \approx 259.7$, set using PyRPL. Noise introduces deviations from 0 V, which the Red Pitaya attempts to compensate for by adjusting the tuning voltage of the VCXO driving the AOM.

The control signal $V_{con}(t)$ from the Red Pitaya is used to adjust the output frequency of the VCXO. Since $V_{con}(t) \in [-1, 1]$ V does not match the tuning voltage range of the VCXO, a differential amplifier is used to shift and rescale the control signal to the correct voltage range. The output $V_{tune}(t)$ of the differential amplifier is then used as a tuning voltage for the VCXO, but not before a low pass filter is used to suppress unwanted high frequency components that were introduced by the differential amplifier.

The VCXO output signal is a square wave, and thus two low pass filters are used to suppress higher harmonics[8] and make it more sinusoidal. The signal power is adjusted to appropriate levels for driving the AOM using an attenuator and an amplifier.

The supply voltage of the VCXO is 3.3 V.

Differential amplifier circuit

A differential amplifier is a circuit that amplifies the difference between two input signals, in this case the control signal $V_{con}(t)$ from the Red Pitaya and a fixed

[8]The bandwidth of the filters is 80 MHz, but the carrier at 100 MHz is barely suppressed while the first harmonic at 200 MHz is suppressed by > 40 dB.

offset of $-1\,\mathrm{V}$. It is implemented[9] using an CA3140EZ operational amplifier and four resistors connected according to figure 8.5. This op-amp is powered by two voltages $V_+ = 15\ \mathrm{V}$ and $V_- = -15\ \mathrm{V}$.

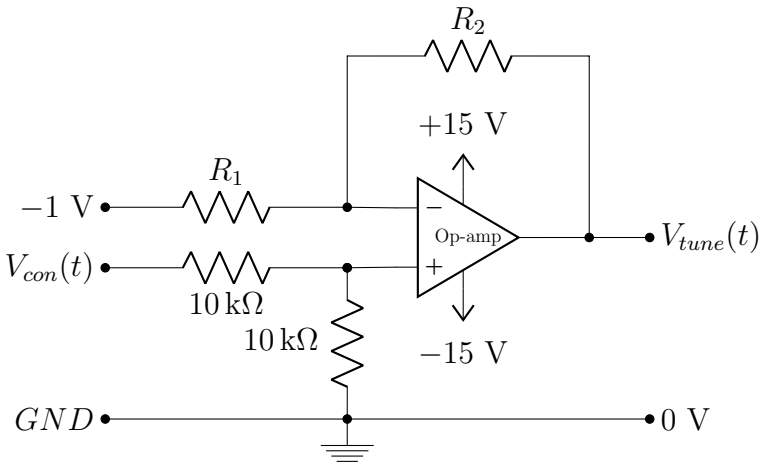

Figure 8.5: The differential amplifier circuit.

The output voltage $V_{tune}(t)$ of this circuit is given by

$$V_{tune}(t) = \frac{R_2}{R_1}(V_{con}(t) + 1\,\mathrm{V}). \tag{8.12}$$

With $R_1 = 10\ \mathrm{k\Omega}$, $R_2 = 15\ \mathrm{k\Omega}$ we can thus rescale the output voltage of the Red Pitaya $V_{con}(t) \in [-1, 1]\ \mathrm{V}$ to $V_{tune}(t) \in [0, 3]\ \mathrm{V}$, which can be used to tune the output frequency of the VCXO.

8.3 Results

The averaged spectrum is shown in figure 8.6 for a 2 kHz span around the center peak. This is for both when the fiber noise cancellation was active and turned off. The inset shows the spectrum for a 100 kHz span.

We can see that there is not much noise to begin with in the setup as it is, but some details can be observed. The fiber noise cancellation does increase the peak of the signal by a few dBm while low frequency noise is suppressed. Since we used the VCXO for both measurements it is not due to driving the AOM at different power, albeit a difference in coupling efficiency could matter. In the inset, however, we can see an increase in the noise further out from the center peak.

[9]The circuit can be found in [23] under the name *difference amplifier*.

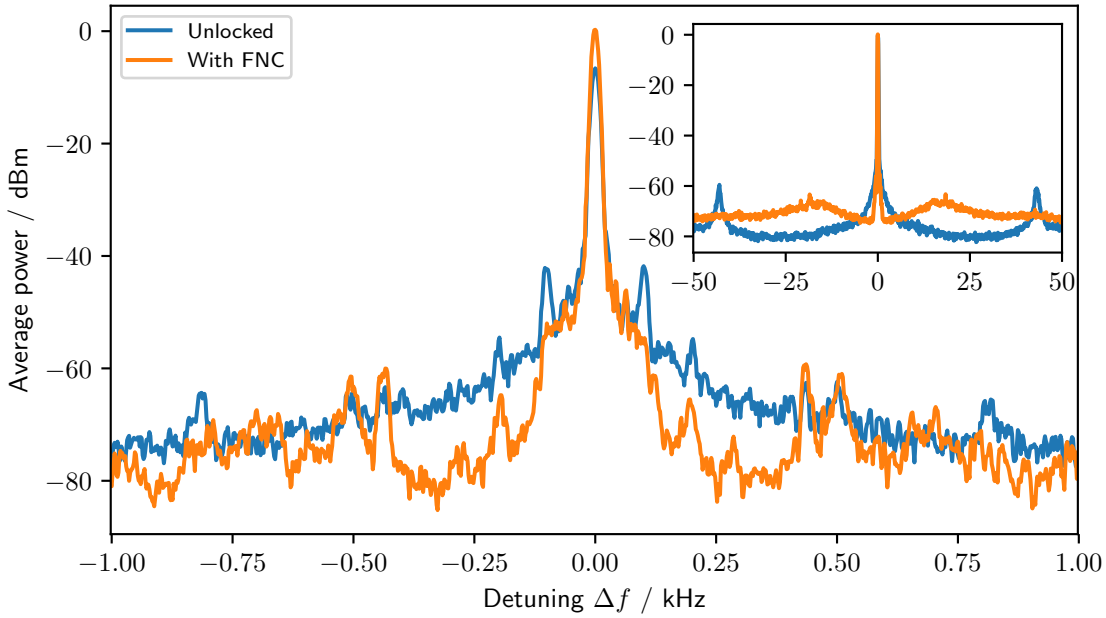

Figure 8.6: Averaged out-of-loop spectrum with and without fiber noise cancellation, with a span of 2 kHz and a resolution bandwidth of 10 Hz. In the inset we used a span of 100 kHz and a resolution bandwidth of 100 Hz instead.

Unfortunately there was not much noise and thus it is hard to say from the measured spectra how well the fiber noise cancellation will perform. In chapter 9 we therefore purposefully introduce noise into the fiber to characterize its performance.

Chapter 9

Characterizing fiber noise cancellation

In this chapter we characterize the fiber noise cancellation more thoroughly by exciting specific frequency components using a speaker placed under the optical fiber.

9.1 Characterizing setup

In order to characterize the performance of the fiber noise cancellation we would use a speaker, positioned under the fiber, to excite specific frequency components in the light passing through the fiber. We used either a smaller[1] or a larger[2] speaker, shown in figure 9.1, depending on the frequencies we characterized. The speaker was connected to a signal generator[3] which could be remote controlled from a computer via USB. To excite a frequency component ω_m we would generate a sinusoidal signal with the speaker, introducing a phase modulation

$$\phi_f(t) = A\sin(\omega_m t + \phi_m) \tag{9.1}$$

with amplitude A and phase ϕ_m into the laser light passing through the fiber through vibrations. A schematic overview of the setup is shown in figure 9.2.

To control each part of the setup we used the Python programming language. For the spectrum analyzer the PyVISA package was used and for the signal generator, the pyserial package was used. PyRPL was used to control the Red Pitaya.

[1] Veco Vansonic 40KS08.
[2] Xindao P326.63.
[3] Rigol DG1022a.

(a) (b) (c)

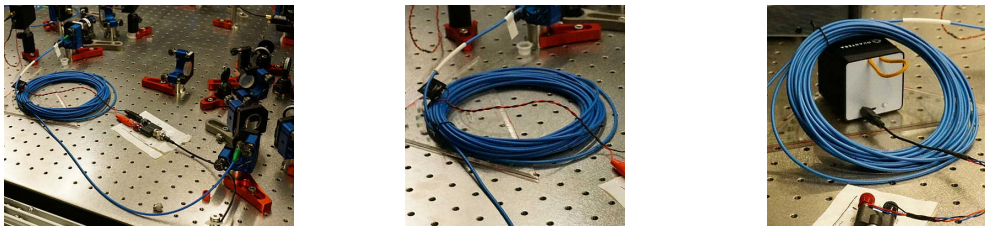

Figure 9.1: The (a)(b) small and (c) large speaker used to excite frequency components ω_m, placed under the fiber.

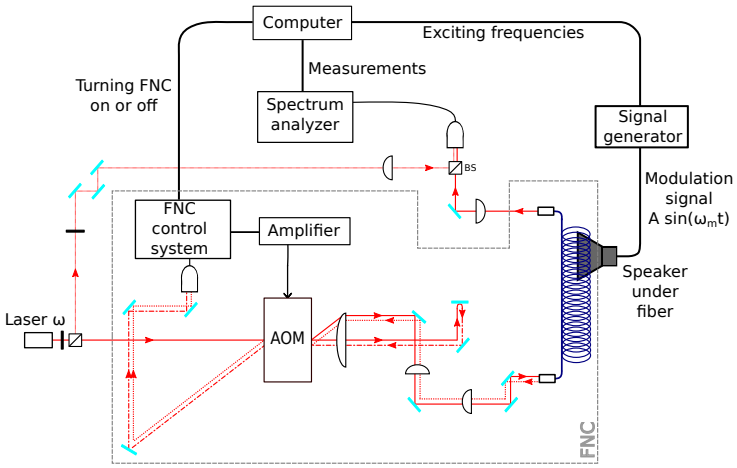

Figure 9.2: Schematic overview of the setup for characterizing the fiber noise cancellation. Frequency components ω_m are excited with a speaker placed under the fiber.

9.1.1 Photodiode signal with a single modulation frequency

To get an idea of how the photodiode signal should look, consider the expression for $I(t)$ in equation (8.10). Defining the time dependence of the beat note term as $f_{beat}(t)$, we can write $I(t)$ as

$$I(t) = I_{-10} + I_{+01} + \frac{1}{2}\sqrt{I_{-10}I_{+01}}f_{beat}(t), \tag{9.2}$$

$$f_{beat}(t) = e^{i(2\omega_{AOM}t - 2\phi_f)} + e^{-i(2\omega_{AOM}t - 2\phi_f)}. \tag{9.3}$$

where Euler's formula was used to express $f_{beat}(t) = 2\cos(2\omega_{AOM}t - 2\phi_f)$ using exponentials. Now consider the special case of a sinusoidal modulation at ω_m

$$-2\phi_f(t) = A\sin(\omega_m t + \phi_m) + \Delta\phi \tag{9.4}$$

where A is the amplitude, ϕ_m the phase of the modulation and $\Delta\phi$ any phase difference between the overlapped laser beams. This gives $f_{beat}(t)$ as

$$f_{beat}(t) = e^{i(2\omega_{AOM}t+\Delta\phi)}e^{iA\sin(\omega_m t+\phi_m)} + e^{-i(2\omega_{AOM}t+\Delta\phi)}e^{-iA\sin(\omega_m t+\phi_m)}.$$

The exponential terms containing the modulation can then be rewritten using the Jacobi-Anger expansion, called the modulation identity in [24], in the form[4]

$$e^{\pm ix\sin\theta} = \sum_{n=-\infty}^{\infty} J_n(x)e^{\pm in\theta}. \tag{9.5}$$

With $x \to A$ and $\theta \to \omega_m t + \phi_m$ we can see that

$$e^{\pm i(2\omega_{AOM}t+\Delta\phi)}e^{\pm iA\sin(\omega_m t+\phi_m)} = e^{\pm i(2\omega_{AOM}t+\Delta\phi)}\sum_{n=-\infty}^{\infty} J_n(A)e^{\pm in(\omega_m t+\phi_m)} =$$
$$= \sum_{n=-\infty}^{\infty} J_n(A)e^{\pm i((2\omega_{AOM}+n\omega_m)t+n\phi_m+\Delta\phi)}$$

and thus

$$\begin{aligned} f_{beat}(t) &= e^{i(2\omega_{AOM}t+\Delta\phi)}e^{iA\sin(\omega_m t+\phi_m)} + e^{-i(2\omega_{AOM}t+\Delta\phi)}e^{-iA\sin(\omega_m t+\phi_m)} = \\ &= \sum_{n=-\infty}^{\infty} J_n(A)\left(e^{i((2\omega_{AOM}+n\omega_m)t+n\phi_m+\Delta\phi)} + e^{-i((2\omega_{AOM}+n\omega_m)t+n\phi_m+\Delta\phi)}\right) = \\ &= 2\sum_{n=-\infty}^{\infty} J_n(A)\cos\left[(2\omega_{AOM}+n\omega_m)t + n\phi_m + \Delta\phi\right] \end{aligned}$$

As such we have found that

$$I(t) = I_{-10} + I_{+01} + \frac{1}{2}\sqrt{I_{-10}I_{+01}}f_{beat}(t),$$
$$f_{beat}(t) = 2\sum_{n=-\infty}^{\infty} J_n(A)\cos\left[(2\omega_{AOM}+n\omega_m)t + n\phi_m + \Delta\phi\right].$$

From this we can see that for a modulation at a given angular frequency ω_m, the beat note spectrum should contain the center peak at $2\omega_{AOM}$ surrounded by series of sidelobes at $n\omega_m$ for $n = \pm1, \pm2, \pm3, ...$ with an amplitude that depends on $\sqrt{I_{-10}I_{+01}}J_n(A)$. The phase term $n\phi_m$ introduces a phase factor that depends on n.

[4] Typically it is expressed as $e^{ix\cos\Theta} = \sum_{n=-\infty}^{\infty} i^n J_n(x)e^{in\Theta}$, but the chosen form is obtained via a different phase $\theta = \Theta + \pi/2$ and noting that $\pm\sin\theta = \sin(\pm\theta)$.

The photodiode signal is then proportional to $I(t)$. It is then filtered and amplified before being mixed down to DC to give the error signal $e(t)$ to the PI controller. The frequency components of the error signal will be at the frequency difference between the photodiode signal and the reference signal, giving us

$$e(t) = K_0 + K_1 \sum_{n=-\infty}^{\infty} J_n(A) \cos\left[n\omega_m t + n\phi_m + \Delta\phi\right]. \tag{9.6}$$

where K_0 is due to any remaining DC voltage and K_1 scales the oscillating terms.

9.1.2 Characterizing performance at different frequencies

The Red Pitaya was connected to the experiment computer via an Ethernet cable, and could be controlled from Python via the PyRPL package. As previously we used the PI parameters $K_p \approx 3.1$ and $K_i \approx 259.7$, set from PyRPL. The measurements were taken using photodiode B connected to the spectrum analyzer, which in turn was connected to the experiment computer via a COM port. A Python script was then used to run a series of measurements, first with the fiber noise cancellation active and then leaving the VCXO unlocked. In both cases the same steps were performed.

To characterize the performance of the PI controller we first choose a number of modulation frequencies ω_m and the desired number N of repeated measurements for each ω_m. Then we find the carrier frequency ω_c of the beat note, which is important since we will be measuring at an offset ω_m from the carrier and thus we need to know the exact frequency of the carrier. The order of the modulation frequencies is then randomized.

We now choose a frequency ω_m. The speaker is used to generate a sinusoidal signal at ω_m, which introduces vibrations into the fiber and thus modulates the optical path length of the laser light in the fiber. This way a phase modulation $\phi_f(t)$ at ω_m is introduced in the laser light. Assuming $\phi_f(t)$ takes the form of equation (9.4) we should, according to section 9.1.1, be able to observe peaks in the spectrum at offsets $n\omega_m$ from the carrier frequency ω_c, where n is a non-zero integer.

Once we have excited a modulation at ω_m we measure the power at the carrier ω_c and then at the first modulation sideband $\omega_c + \omega_m$. The speaker is then turned off, and we measure the power at $\omega_c + \omega_m$ again to get information about the power level without the modulation. The measurements are then saved to a file.

This is repeated N times for a modulation frequency ω_m before continuing with the next ω_m. Close to the carrier care has to be taken to make sure the measurement does not characterize the carrier. Once all measurements are done for all modulation frequencies, the fiber noise cancellation is turned off and we

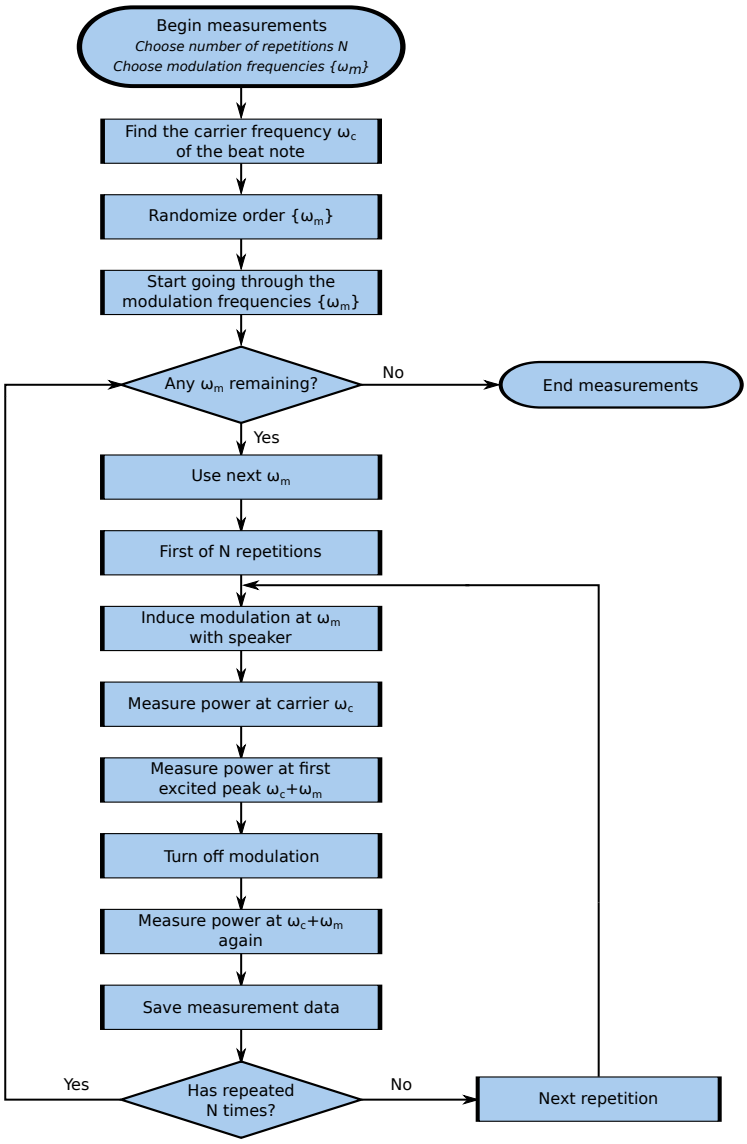

Figure 9.3: Flow chart over the algorithm used for characterizing the fiber noise cancellation (FNC) at different modulation frequencies. ω_m denotes a single modulation frequency, ω_c denotes the carrier frequency and $\{\omega_m\}$ the set of modulation frequencies to characterize. The experiment is initialized with the fiber noise cancellation active, a given set of modulation frequencies $\{\omega_m\}$ and the number N of repeated measurements at each ω_m. Then the sequence of measurements described by the flow chart is run twice. First with the fiber noise cancellation and then without. The measurement data is automatically saved digitally.

repeat the measurements one more time with the VCXO unlocked. When unlocked the VCXO can drift, but these drifts are slow compared to the run time of the experiment. Do note that since the carrier frequency ω_c is not guaranteed to be the same with the VCXO unlocked as with the fiber noise cancellation, we have to find ω_c again.

When the experiment is done we activate the fiber noise cancellation and run the experiment a few more times. Each time first with fiber noise cancellation and then without. Locking the PI controller again currently has to be done manually.

9.1.3 Modulation frequency intervals

We measured 3 intervals. First with 12 evenly spaced frequencies $\omega_m/2\pi \in [1, 10]$ kHz followed by another 12 frequencies in $\omega_m/2\pi \in [300, 1000]$ Hz. These were measured 30 times in total, using the smaller speaker to excite the frequency components. For the final interval we would have 6 evenly space frequencies $\omega_m/2\pi \in [50, 250]$ Hz, each of which was measured a total of 36 times. Since the small speaker was not as effective at these lower frequencies, the larger speaker, depicted in 9.1(c), was used instead.

9.2 Results

By driving the speaker at[5] $\omega_m/2\pi = 872.72$ Hz we could excite frequency components at $n\omega_m$ as shown in figure 9.4, both with and without fiber noise cancellation. We see peaks at $n\omega_m$ for $n = \pm1, \pm2, ..., \pm5$ and with fiber noise cancellation their amplitude is reduced except for furthest peaks.

The results from the measurements described in section 9.1.2 are shown in logarithmic scale in figure 9.5, where $P_{unlocked}$ and P_{FNC} denotes the power of excited peaks at different ω_m. We subtracted the background from $P_{unlocked}$ and P_{FNC} that was measured without the modulation at ω_m. With this method we compare $P_{unlocked}$ and P_{FNC} without being sensitive to any noise offset, as for instance visible in the inset of figure 8.6. Figure 9.5 also shows the power ratio $P_{FNC}/P_{unlocked}$ in dB between when the fiber noise cancellation is active or inactive. We can see that with the fiber noise cancellation the peak amplitudes are reduced, especially for smaller ω_m. At higher ω_m, however, the excited peak amplitude decreases, possibly because these frequencies are not easily transmitted acoustically through the fiber[21]. From figure 9.5(b) we can estimate that the power ratio $P_{unlocked}/P_{FNC}$ drops below 10 dB suppression above $\omega_m/2\pi \approx 4.3$ kHz. For $\omega_m/2\pi \leq 1$ kHz the suppression power ratio is mostly above 20 dB.

[5]This frequency was chosen since the fiber would pick it up easily.

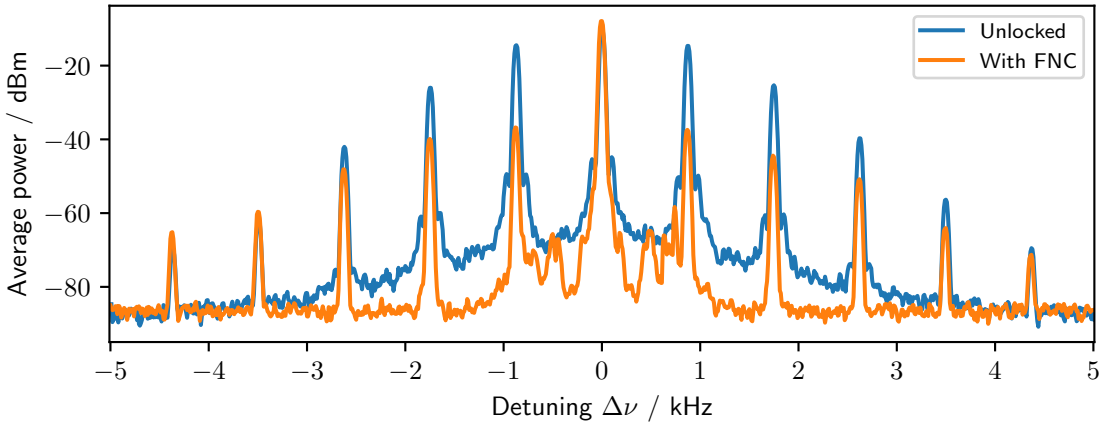

Figure 9.4: Averaged spectrum in 10 kHz span around the center peak at 100 MHz, with a 872.72 Hz sinusoidal signal applied to the speaker.

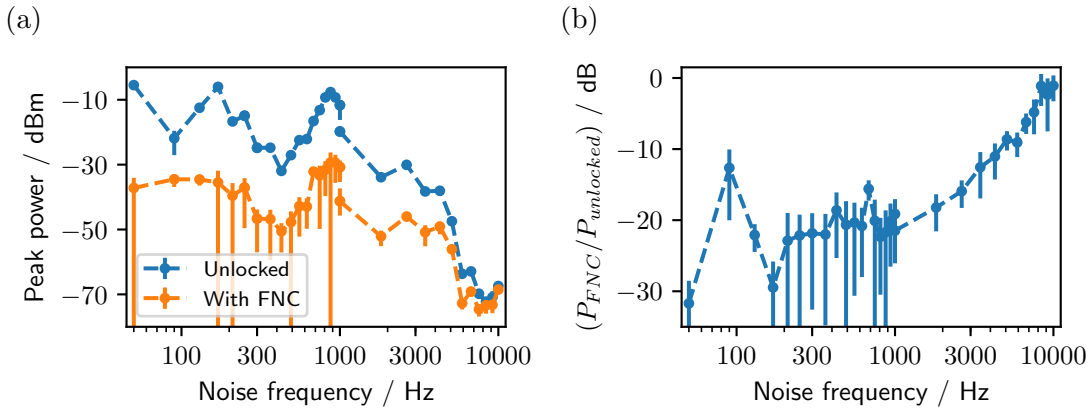

Figure 9.5: The (a) peak power P_{FNC} and $P_{unlocked}$, for with and without the fiber noise cancellation, as well as (b) the power ratio $P_{FNC}/P_{unlocked}$.

Another way to quantify the suppression is by defining the linear[6] suppression $\Delta P/P_{unlocked}$ as the ratio between the power difference and the power of the unlocked peak at ω_m. $\Delta P/P_{unlocked}$ is close to unity as long as the power at ω_m is much lower with the lock compared to without, but reduces when they become roughly the same order of magnitude. At $\Delta P/P_{unlocked} = 0$ the lock has no effect and if $\Delta P/P_{unlocked} < 0$ then the lock increases noise instead. $\Delta P/P_{unlocked}$ is shown in figure 9.6 for the measurements. We can see that $\Delta P/P_{unlocked}$ drops below 0.9 and 0.5 at $\omega_m/2\pi \approx 4.3\,\text{kHz}$ and $\omega_m/2\pi \approx 7.5\,\text{kHz}$, respectively. However, the peaks have dropped significantly in amplitude at this point and the the error bars have become large.

[6]This is referred to as *linear* since we use mW rather then dBm for the powers.

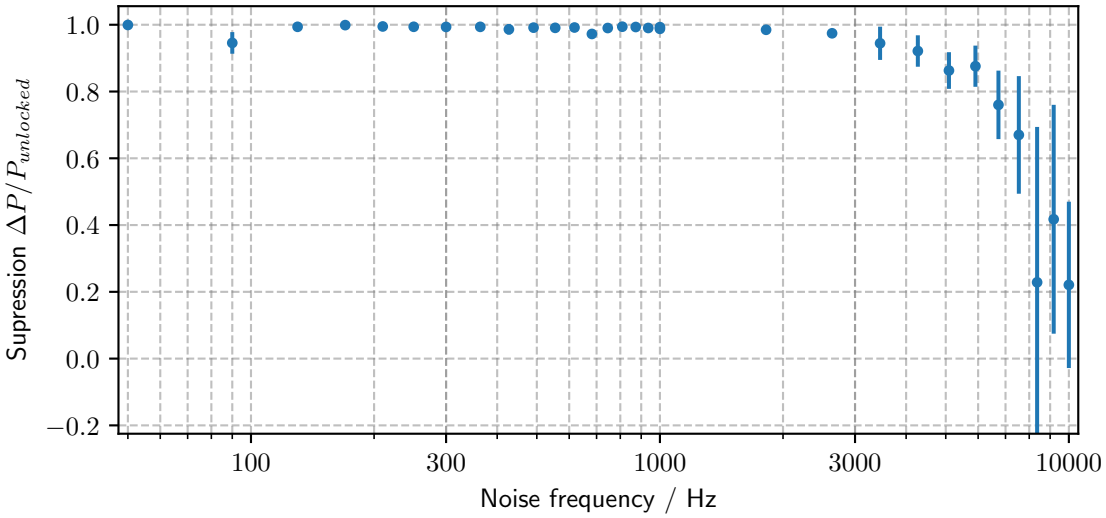

Figure 9.6: Linear suppression $\Delta P/P_{unlocked}$, where $\Delta P = P_{unlocked} - P_{FNC}$.

Chapter 10

Discussion: Fiber noise cancellation

We have implemented a fiber noise cancellation scheme using a Red Pitaya as a PI controller. To characterize the performance of this scheme we used speakers to excite frequency components through phase modulation. From this characterization we could see that the system could effectively suppress fiber noise by more then 10 dB up to 4.3 kHz, corresponding to a linear suppression of $> 90\,\%$. Below 1 kHz the suppression was typically better then 20 dB.

The characterization method we employed could additionally be improved by using sound level meter and a pressure sensor to determine the sound level and air pressure at the fiber due to the speakers. This was done in [21]. We would get more information about how the speaker affect the fiber, and thus we could better distinguish between where the speaker is less efficient and where the fiber does not pick up acoustic vibrations.

10.1 Improvements to the fiber noise cancellation

The current system appears to work well, but some improvements can still be suggested. For the PI controller there is room to further optimize the PI parameters, which could yield better performance and reliability. Other then that we could also improve the electronics. A more careful design of the circuits could help eliminate noise introduced by the electronics. This is not known to be a problem at the moment, but it is something to be aware of for going forward. We could also design an integrated circuit containing the electronics, which has been done successfully before [20].

10.1.1 Overcoming the limitations of the Red Pitaya DAC

Currently we employ a Red Pitaya as a PI controller. It has an 14 bit digital-to-analog converter (DAC) allowing it to adjust the output voltage in steps of $2/2^{14}$ V. The Red Pitaya was able to tune the VCXO output frequency in a frequency range of $\approx 23.4\,\mathrm{kHz}$. Thus the system should be able to adjust the output frequency in steps of $23.4\,\mathrm{kHz}/2^{14} \approx 1.43\,\mathrm{Hz}$. It is desirable to get linewidths of 1 Hz or lower, but this is might not feasible with the Red Pitaya and the current VCXO.

Alternatively we could switch to a VCXO with lower tuning range to get around this, but this would limit the fiber noise cancellation efficiency for higher frequencies. Whether this poses a problem depends on the phase noise introduced by the fibers.

Another option is to use a different PI controller with a higher resolution DAC. Keep in mind that every extra bit for the DAC doubles the resolution, so even 15 bits would improve performance. If we wish to retain the tuning range of the VCXO, or perhaps even increase it, then a different PI controller is likely required. Alternatively a different kind of control system, such as a Phase-Locked Loop[23], could be used.

Chapter 11

Summary and outlook

In this thesis we have setup two systems for improving the coherence times of trapped ion qubits.

We have replaced the previously used coils by two frames, each of which containing 60 Sm_2Co_{17} permanent magnets. They were mounted at the same place as previously the coils and have been adjusted to be separated by $\approx 25\,\mathrm{cm}$ to be in a Helmholtz-like configuration and produce a homogeneous magnetic field. We measured the magnetic field to be $B \approx 3.46\,\mathrm{G}$ and magnetic field gradients of $\partial B_{m+c}/\partial z = -91.1 \pm 2.0$ µG/µm and $\partial B_m/\partial z = -89.1 \pm 2.5$ µG/µm, depending on if the compensation coils were used or not.

Coherence times were unfortunately not improved, which is consistent with previous results from other groups[2] where they found that a magnetic field shielding is required for substantial coherence time improvements. We are likely limited by noise from external magnetic fields generated by the electrical devices in the lab, or possibly from other labs that utilize strong magnets. A magnetic field shielding has arrived but has yet to be installed in the experiment.

We estimated the RMS of the magnetic field and laser frequency fluctuations to be $\sqrt{\overline{\Delta B^2}} \approx 110\,\mu\mathrm{G}$ and $\sqrt{\overline{\Delta\omega^2}} \approx 2\pi \times 100\,\mathrm{Hz}$, respectively. These results can likely be improved utilizing entangled or correlated states, which has previously been used to measure laser linewidth[19].

To improve coherence, a magnetic field shielding is required. Further improvements can be made by possibly replacing the 3D printed magnet holders with aluminium magnet holders. The magnetic field gradient can possibly be improved by tweaking the magnet holder separation and how many magnets are on each holder. Additionally, magnetic field stability may be improved using several different types of permanent magnets to compensate for temperature effects.

We have also implemented a test setup for fiber noise cancellation, using a Red Pitaya as PI controller. The current setup can likely be significantly improved, but it appears to be able to effectively cancel fiber noise up to a few kHz. This can

likely be improved with a dedicated integrated circuit, as well as by optimizing the PI parameters more and with a PI controller with a DAC with more bits. Alternatively a PLL might be an alternative to a PI controller.

In short, the next steps for improved coherence times should be to implement the fiber noise cancellation in the ion trap experiment and to add the magnetic field shielding. The fiber noise cancellation should be easier to implement, but if magnetic field fluctuations are the limiting factor then the most significant improvement likely comes from the magnetic field shielding.

It is possible[25] to use spin-echo measurements with more then one π-pulse between the initial and final $\pi/2$-pulses to investigate the noise spectrum. If these techniques could be adapted to our experiment, it would allow us to identify at what frequencies we have noise, which could help identifying noise sources and figuring out how to avoid them.

Appendix A

The Bloch sphere

This appendix aims to give an introduction to the Bloch sphere for the unfamiliar reader. For more information I refer to [1][26], which were used in writing this appendix.

A.1 The Bloch sphere

The computational basis for a single qubit $|\psi\rangle$ is $|0\rangle$ and $|1\rangle$. In general the qubit can be written as a linear combination $|\psi\rangle = c_0|0\rangle + c_1|1\rangle$ where c_0 and c_1 are complex coefficients subject to the normalization condition $|c_0|^2 + |c_1|^2 = 1$.

The normalization condition of c_0 and c_1 implies that the possible qubit states $|\psi\rangle$ can have a geometric interpretation. Specifically, let us rewrite c_0 and c_1 using two angles θ and ϕ as

$$c_0 = \cos\left(\frac{\theta}{2}\right),$$
$$c_1 = e^{i\phi}\sin\left(\frac{\theta}{2}\right).$$

Then $|\psi\rangle$ becomes[1]

$$|\psi\rangle = \cos\left(\frac{\theta}{2}\right)|0\rangle + e^{i\phi}\sin\left(\frac{\theta}{2}\right)|1\rangle. \tag{A.1}$$

Written in this way we can interpret θ and ϕ as the *polar angle* and *azimuthal angle* of a point on a unit sphere called the *Bloch sphere*. An angle $\theta = 0$ describes a

[1]It should be noted that $|\psi\rangle$ should technically be multiplied with an extra phase factor $e^{i\gamma}$ to be more general. However, this phase factor has no measurable effect and for this reason it is neglected here.

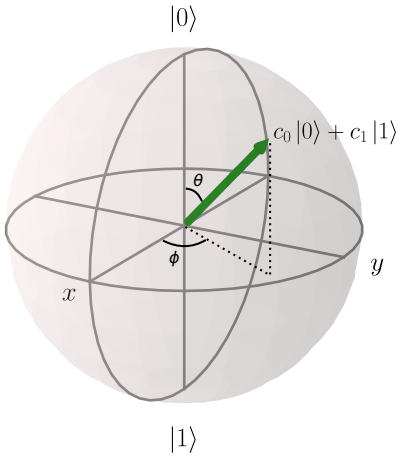

Figure A.1: Bloch sphere representation of a state where $c_0 = \cos(\pi/8)$ and $c_1 = e^{i\pi/2}\sin(\pi/8)$, corresponding to $\theta = \pi/4$ and $\phi = 2\pi/5$ from equation (A.1).

pure $|0\rangle$ state while $\theta = \pi$ describes a pure $|1\rangle$ state. These become the north and south poles of the Bloch sphere. Intermediate θ along with $0 \leq \phi < 2\pi$ describe all other states. The equator on the Bloch sphere has $\theta = \pi/2$ and contains all states

$$|\psi\rangle = \frac{1}{\sqrt{2}}|0\rangle + \frac{e^{i\phi}}{\sqrt{2}}|1\rangle. \tag{A.2}$$

These states, with $\theta = \pi/2$, represents states where $|\psi\rangle$ is equally probable to be measured in $|0\rangle$ as in $|1\rangle$. Two special cases of these states are the $|+\rangle$ and $|-\rangle$ states, corresponding to $\phi = 0$ and $\phi = \pi$ respectively. In other words

$$|\pm\rangle = \frac{1}{\sqrt{2}}\left(|0\rangle \pm |1\rangle\right). \tag{A.3}$$

The vector describing the position of the state on the Bloch sphere is called the *Bloch vector*. In polar coordinates the Bloch vector ψ corresponding to the state $|\psi\rangle$ would be $\psi = (r, \theta, \phi)$, where $r = |\psi|$ is the length of the Bloch vector. It may of course be represented in Cartesian coordinates as well. By convention, the z axis is then said to be the axis aligned with the $|0\rangle$ and $|1\rangle$ states. The x and y axis are somewhat arbitrary, except that they lie in the equatorial plane of the Bloch sphere and are orthogonal to each other.

There is a time dependence in the Bloch vector due to the intrinsic angular frequency ω_0 of a two level quantum system. As a result the Bloch vector rotates at an angular frequency ω_0. Usually, however, a rotating frame is chosen as basis and as such we do not have to consider this rotation.

In our case, the qubit is represented as two energy levels in a strontium ion. The angular frequency of this transition is the ω_0 discussed above. The electronic state is then manipulated using lasers with an angular frequency ω which might be close but not equal to ω_0. In other words, we have $\omega \approx \omega_0$. Such a light field causes the Bloch vector to rotate, even in the rotational basis of the qubit. Specifically it will slowly rotate around the z axis with angular frequency $\Delta\omega = \omega - \omega_0$. Technically the interaction also allows the possibility for the Bloch vector to rotate at $\omega + \omega_0 \approx 2\omega_0$, but this would be highly non-resonant and can be neglected. Neglecting $\omega + \omega_0$ is called the rotating wave approximation.

One thing to note with the Bloch sphere is that orthogonal states are anti-parallel when represented on the Bloch sphere. $|0\rangle$ and $|1\rangle$ appear as the north and south pole, along the same axis on the Bloch sphere. The vectors representing them would, however, be anti-parallel.

A.2 Unitary operations and rotations of qubits

A unitary operation U on a qubit state $|\psi\rangle$ can be considered as a rotation. On the Bloch sphere this can be seen directly, since unitary operations corresponds to rotating the Bloch vector. This is commonly used in quantum computation and quantum information to illustrate what a unitary operation does to a single qubit.

Consider a case where we have prepared the qubit in state $|1\rangle$. If we then apply a unitary operation $U_{\pi/2}$ that transforms $|1\rangle$ into $|+\rangle$, then on the Bloch sphere we have rotated the Bloch vector from the north $|1\rangle$ state to the equatorial $|+\rangle$ state. This corresponds to a rotation of $\pi/2$ radians of the Bloch vector and is called a $\pi/2$-*pulse*. Similarly a unitary operation U_π that takes the state from $|1\rangle$ to $|0\rangle$ would be called a π-*pulse*, since it rotates the Bloch vector by π radians around the equator. In general, if a unitary operation rotates the state by Θ radians, then it is called a Θ-pulse[2].

It should be noted that not all operations will conserve the length of the Bloch vector. In particular dephasing processes effectively shrinks the Bloch vector in x and y direction due to averaging over different phases ϕ. This is a statistical phenomenon due to how repeated operations can accumulate different amount of phase and thus give different results. When averaged these results give an effectively smaller Bloch vector due to superposition states transforming into *statistical mixtures*.

Other damping processes then dephasing can be imagined as other deformations of the Bloch sphere [1].

[2]Here Θ is just a placeholder for an angle, not part of the name.

Appendix B

Average of a noisy exponential

This appendix derives equation (6.11). To do so we make a Taylor expansion of $\exp(-2i\phi(t))$, where $\phi(t) = \frac{1}{2\hbar}\int_0^t dt'\,\Delta E(t')$ and $\Delta E(t)$ is a Gaussian process. This gives us

$$\overline{\exp(-2i\phi)} = \sum_{n=0}^{\infty} \frac{(-2i)^n \overline{\phi^n}}{n!} = \sum_{k=0}^{\infty} \frac{(-4)^k \overline{\phi^{2k}}}{(2k)!} + \sum_{k=0}^{\infty} \frac{(-2i)^{2k+1} \overline{\phi^{2k+1}}}{(2k+1)!} \tag{B.1}$$

where in the last step we split up the Taylor expansion in even and odd terms. Since $\Delta E(t)$ is a Gaussian process we can apply the Gaussian moment theorem[18] on the terms $\overline{\phi^{2k}}$ and $\overline{\phi^{2k+1}}$. For even terms we get that $\overline{\phi^{2k}} = (2k-1)!!\overline{\phi^2}^k$, where $(2k-1)!!$ is the semifactorial, while for the odd terms $\overline{\phi^{2k+1}} = 0$. Equation (B.1) then becomes

$$\overline{\exp(-2i\phi)} = \sum_{k=0}^{\infty} \frac{(-2i)^{2k}(2k-1)!!\overline{\phi^2}^k}{(2k)!} \tag{B.2}$$

For an integer $m \geq 0$ we have that $m!! = m!/(m-1)!!$. Additionally for an even integer $m = 2k$, where $k \geq 0$, we can express the semifactorial as $m!! = 2^k k!$. Using these we can determine that

$$\frac{(2k-1)!!}{(2k)!} = \frac{1}{(2k)!!} = \frac{1}{2^k k!}. \tag{B.3}$$

Combining equations (B.2) and (B.3) finally gives us

$$\overline{\exp(-2i\phi)} = \sum_{k=0}^{\infty} \frac{(-4)^k \overline{\phi^2}^k}{2^k k!} = \sum_{k=0}^{\infty} \frac{(-2\overline{\phi^2})^k}{k!} = \exp\left(-2\overline{\phi^2}\right). \tag{B.4}$$

Acknowledgments

This thesis would not have been possible without the help of some patient people that I would like to thank in no particular order. I would like to thank my supervisor, Markus Hennrich, as well as the assistant supervisor, Dr Gerard Higgins, and PhD students Fabian Pokorny and Chi Zhang for all their help and patience. Furthermore I would like to thank Tiffany Brydges from the University of Innsbruck and Ulrich Poschinger from the University of Mainz for their invaluable guidance regarding the permanent magnets.

I would like to thank Attila Hidvegi and Matthias Hudl Waltin from the technical division at Stockholm University for their help with the fiber noise cancellation electronics and optics.

Finally I would like to thank my parents for their support and patience.

Bibliography

[1] Michael A. Nielsen and Isaac L. Chuang. *Quantum Computation and Quantum Information: 10th Anniversary Edition.* Cambridge University Press, 2011.

[2] T. Ruster, C. T. Schmiegelow, H. Kaufmann 1, C. Warschburger, F. Schmidt-Kaler, and U. G. Poschinger. A long-lived Zeeman trapped-ion qubit. *Applied Physics B*, 122:254–261, September 2016.

[3] Stephen M. Barnett. *Quantum Information.* Oxford University Press, 2009.

[4] Christopher J. Foot. *Atomic Physics.* Oxford University Press, 2005.

[5] Christian Felix Roos. *Controlling the quantum state of trapped ions.* PhD thesis, University of Innsbruck, February 2000.

[6] Fabian Pokorny. Experimental setup for trapping strontium rydberg ions. Master's thesis, Leopold-Franzens University of Innsbruck, March 2014.

[7] Thomas Monz, Philipp Schindler, Julio T. Barreiro, Michael Chwalla, Daniel Nigg, William A. Coish, Maximilian Harlander, Wolfgang Hänsel, Markus Hennrich, and Rainer Blatt. 14-Qubit Entanglement: Creation and Coherence. *Physical Review Letters*, 106:130506, April 2011.

[8] Eric D. Black. An introduction to Pound–Drever–Hall laser frequency stabilization. *American Journal of Physics*, 69:79–87, 2001.

[9] Long-Sheng Ma, Peter Jungner, Jun Ye, and John L. Hall. Delivering the same optical frequency at two places: accurate cancellation of phase noise introduced by an optical fiber or other time-varying path. *Optics Letters*, 19(21):1777–1779, November 1994.

[10] Tai L. Chow. *Introduction to Electromagnetic Theory: A Modern Perspective.* Jones & Bartlett Learning, 2006.

[11] Janine Nicodemus. Automated positioning control for trapped-ion quantum registers. Master's thesis, Johannes Gutenberg University of Mainz, October 2017.

[12] I. S. Grant and W. R. Phillips. *Electromagnetism*. Wiley, 2nd edition, 1991.

[13] H. Häffner. private communication.

[14] Glen Cowan. *Statistical Data Analysis*. Oxford University Press, 1998.

[15] Mark Riebe. *Preparation of Entangled States and Quantum Teleportation with Atomic Qubits*. PhD thesis, University of Innsbruck, May 2005.

[16] Gerard Higgins. *A single trapped Rydberg ion*. PhD thesis, Stockholm University, March 2018.

[17] Thomas Monz. *Quantum information processing beyond ten ion-qubits*. PhD thesis, University of Innsbruck, August 2011.

[18] Leonard Mandel and Emil Wolf. *Optical coherence and quantum optics*. Cambridge University Press, 1995.

[19] Michael Chwalla. *Precision spectroscopy with $^{40}Ca^{+}$ ions in a Paul trap*. PhD thesis, University of Innsbruck, April 2009.

[20] N. Darkwah Oppong. Cancelation of optical phase noise induced by an optical fiber. Internship report, ETH Zürich, 2015.

[21] Long-Sheng Ma, Peter Jungner, Jun Ye, and John L. Hall. Accurate cancellation (to milliHertz levels) of optical phase noise due to vibration or insertion phase in fiber transmitted light. In Yaakov Shevy, editor, *Laser Frequency Stabilization and Noise Reduction*, volume 2378, pages 165 – 175. International Society for Optics and Photonics, April 1995.

[22] Karl Johan Åström and Richard M. Murray. *Feedback Systems: An Introduction for Scientists and Engineers*. Princeton University Press, 2009.

[23] Paul Horowitz and Winfield Hill. *The Art of Electronics*. Cambridge University Press, 2015.

[24] Daniel A. Steck. Classical and modern optics. available online, June 2006. revision 1.7.4, 6 July 2017.

[25] Shlomi Kotler, Nitzan Akerman, Yinnon Glickman, Anna Keselman, and Roee Ozeri. Single-ion quantum lock-in amplifier. *Nature*, 473:61–65, 2011.

[26] Mark Fox. *Quantum Optics: An Introduction (Oxford Master Series in Physics)*. Oxford University Press, 2006.